A&A, 715, A225 (2026)
https://doi.org/10.1051/0004-6361/202661753
© The Authors 2026

Astronomy & Astrophysics

Internal structure, not environment, shapes metallicity gradients in low-mass galaxies from MaNGA

Anuroop Dasgupta[1,2,3,⋆], Namrata Roy[4,6], Saumyadip Samui[5,⋆], Ritaban Chatterjee[5,⋆], and Fuyan Bian[1]

[1] European Southern Observatory, Alonso de Córdova 3107, Casilla 19001, Vitacura, Santiago 19, Chile
[2] Instituto de Estudios Astrofísicos, Facultad de Ingeniería y Ciencias, Universidad Diego Portales, Av. Ejército Libertador 441, Santiago, Chile
[3] Department of Physics, Presidency University, 86/1 College Street, Kolkata 700073, India
[4] School of Earth and Space Exploration, Arizona State University, Tempe, AZ 85287, USA
[5] School of Astrophysics, Presidency University, 86/1 College Street, Kolkata 700073, India
[6] Raman Research Institute, C. V. Raman Avenue, Sadashivanagar, Bangalore 560080, India

Received 1 July 2026 / Accepted 28 September 2026

ABSTRACT

Context. Dwarf and low-mass galaxies are highly sensitive to stellar feedback and gas flows, yet their spatially resolved gas-phase metallicity remains poorly characterised for lack of large homogeneous integral field spectroscopy samples.
Aims. We measure radial gas-phase metallicity gradients for the largest MaNGA low-mass sample to date and investigate the physical processes governing their chemical enrichment.
Methods. We assembled 382 star-forming low-mass galaxies from MaNGA Data Release 17, spanning $7.2 \leq \log(M_\star/M_\odot) \leq 9.1$ and $z \leq 0.05$. Spectra were stacked in elliptical radial bins and the gas-phase metallicity was derived from the N2 index. After removing the primary dependence on the local stellar mass surface density, $\Sigma_\star$, we defined a residual metallicity, ΔZ, to isolate secondary dependencies.
Results. Metallicity gradients are flat on average (median slope -0.007 dex R_e^{-1}). The residual gradients correlate most strongly with the light concentration (Pearson $r = 0.304$, $r^2 = 0.092$, $p < 0.001$) and gas velocity dispersion ($r = 0.204$, $p < 0.001$), though both are modest predictors accounting for at most 9 percent of the variance. The velocity dispersion result should be interpreted with caution given its sensitivity to spatial resolution. The stellar mass shows no significant Pearson correlation, the large-scale environment shows no significant correlation in either test, and the star formation rate shows only a marginal correlation ($r = 0.106$, $p = 0.042$).
Conclusions. The concentration correlation is robust to measurement uncertainties and persists when a stricter spatial resolution cut is applied, suggesting that internal structural properties may play a role in shaping the radial distribution of metals in low-mass galaxies. However the modest effect sizes indicate that no single parameter can fully account for the observed diversity in metallicity gradients, and larger samples will be needed to fully characterise the drivers of chemical enrichment in this mass regime.

Key words. galaxies: abundances – galaxies: dwarf – galaxies: evolution – galaxies: ISM – galaxies: statistics – techniques: spectroscopic

1. Introduction

The chemical evolution of galaxies is one of the central problems in extragalactic astrophysics. As galaxies form stars from their gas reservoirs, successive generations of stellar nucleosynthesis progressively enrich the interstellar medium with heavy elements. At the same time, stellar feedback in the form of supernova-driven winds can expel enriched material into the circumgalactic medium, and accretion of pristine gas from the cosmic web can dilute the existing metal content (Maiolino & Mannucci 2019). The net result of these competing processes is encoded in the gas-phase metallicity of galaxies, commonly measured as the oxygen abundance 12 + log(O/H), which serves as a powerful integrated tracer of a galaxy's star formation history, gas inflow and outflow history, and chemical enrichment (Maiolino & Mannucci 2019). The most direct manifestation of this enrichment at the population level is the mass-metallicity relation (MZR; Tremonti et al. 2004), which establishes that more massive galaxies are on average more metal-rich, a trend that has now been confirmed across a wide range of redshifts and environments (Mannucci et al. 2010; Kewley & Ellison 2008). While the MZR captures the global enrichment level of galaxies, it cannot reveal how metals are distributed spatially within them. Spatially resolved measurements of gas-phase metallicity, made possible by integral field spectroscopy, have opened a new window onto the physical processes that drive chemical enrichment across the discs of galaxies (Sánchez 2020).

The radial gradient of gas-phase metallicity within a galaxy, typically quantified as the slope of the 12 + log(O/H) profile, encodes information about the dominant physical processes shaping chemical evolution. Negative gradients, where the central regions are more metal-rich than the outskirts, are the natural expectation from inside-out disc growth, in which star formation proceeds first in the central regions and gradually extends outwards over time (Matteucci & Francois 1989; Boissier & Prantzos 1999). The first systematic measurements of metallicity gradients in nearby spiral galaxies were obtained from observations of H II regions, establishing that negative gradients of typically -0.1 to -0.2 dex R_e^{-1} are common in massive late-type galaxies (Zaritsky et al. 1994; Moustakas et al. 2010).

⋆ Corresponding authors: anuroop.dasgupta@mail.udp.cl, saumyadip.astro@presiuniv.ac.in, ritaban.astro@presiuniv.ac.in

Open Access article, published by EDP Sciences, under the terms of the Creative Commons Attribution License (https://creativecommons.org/licenses/by/4.0), which permits unrestricted use, distribution, and reproduction in any medium, provided the original work is properly cited.
This article is published in open access under the Subscribe to Open model. Subscribe to A&A to support open access publication.

The advent of integral field spectroscopy surveys brought a dramatic improvement in both sample size and spatial coverage. Using data from the CALIFA survey, Sánchez et al. (2014) showed that the metallicity gradient of isolated spiral galaxies is remarkably uniform at approximately $-0.1\,\mathrm{dex}\,R_e^{-1}$, independent of stellar mass, morphology, and absolute magnitude. Subsequent work with MaNGA confirmed this picture for massive star-forming galaxies ($\log(M_\star/M_\odot) \gtrsim 10$), while revealing that gradients flatten towards both lower masses ($\log(M_\star/M_\odot) \lesssim 9$) and higher masses ($\log(M_\star/M_\odot) \gtrsim 11$) (Belfiore et al. 2017), and that beam smearing from the point spread function can artificially flatten gradients in poorly resolved galaxies (Acharyya et al. 2020). These surveys also established a spatially resolved MZR, in which local gas-phase metallicity correlates with local stellar mass surface density, $\Sigma_\star$, indicating that chemical enrichment is regulated on local scales within galaxies (Rosales-Ortega et al. 2012; Sánchez et al. 2013; Barrera-Ballesteros et al. 2016). Metallicity gradients are also sensitive to dynamical perturbations. Merging and interacting systems bring in fresh, metal-poor gas that can drive the metallicity gradient to be more negative, while the radial mixing of metals over time and feedback-driven outflows tend to redistribute metals across the interstellar medium, making the gradient flatter or even slightly positive (Rupke et al. 2010; Kewley et al. 2010). The balance of these competing processes sets the observed gradient, motivating the search for the physical drivers of gradient diversity that is the focus of this work.

While metallicity gradients in massive galaxies are relatively well characterised, the situation is considerably less clear for dwarf galaxies, i.e. galaxies with stellar masses below $10^9\,M_\odot$. Dwarf galaxies occupy a qualitatively different physical regime from their massive counterparts. Their shallow gravitational potential wells make them highly susceptible to supernova-driven feedback, which can launch large-scale galactic winds capable of expelling enriched gas from the entire disc rather than merely redistributing it radially (Veilleux et al. 2005; Samui et al. 2008; Tolstoy et al. 2009). As a consequence, the inside-out growth scenario that naturally produces negative metallicity gradients in massive galaxies may be fundamentally disrupted in dwarfs, where feedback driven outflows and inflows can mix and even invert intrinsic metallicity gradients built up by spatially concentrated star formation. Cosmological hydrodynamical simulations of dwarf galaxies generally predict weak gas-phase metallicity gradients, with a large galaxy-to-galaxy scatter driven by the bursty and irregular nature of star formation in shallow potential wells (Mercado et al. 2021). Furthermore, dwarf galaxies are more susceptible to environmental processes such as tidal interactions and ram pressure stripping, which can further redistribute gas and metals (Boselli et al. 2022).

Observational studies of spatially resolved gas-phase metallicity in dwarf galaxies have until recently been limited to small samples. The advent of integral field spectrographs on large telescopes enabled the first resolved metallicity maps of dwarf galaxies, though initial studies were necessarily limited to small numbers of objects. Grossi et al. (2020) used integral field spectroscopy of two Virgo cluster dwarf galaxies ($\log(M_\star/M_\odot) \sim 8{-}9$) to derive metallicity maps and radial profiles, finding inverted, positive gradients that they attributed to recent merging and the inflow of metal-poor gas. At the low-mass end, Belfiore et al. (2017) found that the metallicity gradients in MaNGA galaxies lie roughly flat at $\log(M_\star/M_\odot) \sim 9.0$, which suggests that the flattening continues towards lower masses into the dwarf regime. Recent dedicated studies using MUSE and SAMI have begun to extend this to lower masses (Poetrodjojo et al. 2021; Li et al. 2025; Valé et al. 2025), but samples remain small or limited to $\log(M_\star/M_\odot) \gtrsim 8.5$. Despite these advances, the physical drivers of metallicity gradient diversity in low-mass galaxies remain poorly constrained, in particular the relative roles of internal feedback mechanisms and external environmental processes. These can be probed observationally through proxies such as light concentration, morphology, gas velocity dispersion, star formation activity, and the large-scale environment. A large, homogeneous sample of low-mass galaxies with reliable spatially resolved metallicity measurements is needed to make progress on these questions.

In this paper we present the largest sample of dwarf galaxies assembled from the complete Data Release 17 of the MaNGA integral field spectroscopy survey. We select 382 star-forming dwarf galaxies with stellar masses of $M_\star < 10^{9.1}\,M_\odot$, absolute magnitudes of $M_g > -18.5$, and redshifts of $0.01 \leq z \leq 0.05$, closely following the selection criteria of the MaNGA Dwarf Galaxy Sample (MaNDala; Cano-Díaz et al. 2022). Whereas MaNDala selected 136 galaxies at random from those passing these criteria, leaving the low-mass regime sparsely sampled, we apply the criteria to the full survey to obtain a substantially larger and more complete census. For each galaxy we extract elliptically binned, inverse variance weighted stacked spectra in up to ten radial bins, fit the Hα, [N II], Hβ, and [O III] emission lines simultaneously using Gaussian profiles, and derive gas-phase metallicity using the N2 calibration of Pettini & Pagel (2004). We characterise the radial metallicity profiles of the sample and investigate the dependence of metallicity and its radial gradient on the local stellar mass surface density, light concentration, gas velocity dispersion, star formation rate, and large-scale environment, to identify the primary physical drivers of chemical enrichment in this mass regime. This paper is organised as follows. Section 2 describes the data and sample selection. Section 3 describes the analysis pipeline. Section 4 presents the results. Section 5 discusses the physical interpretation. Section 6 summarises our conclusions.

2. Data and sample

2.1. The MaNGA survey

The Mapping Nearby Galaxies at Apache Point Observatory (MaNGA; Bundy et al. 2015) survey is one of the primary programmes of the Sloan Digital Sky Survey IV (SDSS-IV; Blanton et al. 2017). MaNGA used integral field spectroscopy to observe over 10 000 nearby galaxies with a dedicated 2.5 m telescope at the Apache Point Observatory (Gunn et al. 2006), using hexagonal fibre bundle integral field units of 19 to 127 fibres, each fibre subtending 2″ (Drory et al. 2015). The survey provides spectral coverage from 3600 to 10 300 Å at a resolution of $R \sim 2000$ (Smee et al. 2013), with each galaxy observed out to 1.5 or 2.5 effective radii (Law et al. 2015). The data products used here are the LOGCUBE files from the MaNGA Data Reduction Pipeline (DRP; Law et al. 2016), specifically the HYB10-MILESHC-MASTARHC2 version from Data Release 17 (Abdurro'uf et al. 2022). Each LOGCUBE file contains the observed flux cube (`FLUX`) in units of 10^{-17} erg s^{-1} cm^{-2} Å^{-1} per spaxel, the inverse variance (`IVAR`, the reciprocal of the variance per spaxel used to weight spectral fits), a bitmask (`MASK`, where a value of zero indicates a valid uncontaminated spaxel), a log-spaced wavelength array (`WAVE`), and the best-fit stellar continuum (`STELLAR`) from the MaNGA Data Analysis Pipeline (DAP; Westfall et al. 2019), with a spaxel scale of 0.5″.

2.2. Sample selection

We selected the largest sample of dwarf galaxies to date from Data Release 17 of the MaNGA survey. We started from the full MaNGA DR17 sample of 11 273 galaxies and applied a series of quality, redshift, mass, and resolution cuts to define a sample suitable for spatially resolved metallicity analysis. We first required a clean data reduction flag (`drp3qual` = 0), which reduced the sample to 7229 galaxies. We then restricted the redshift range to $0.01 \leq z \leq 0.05$ and adopted a stellar mass cut, $\log(M_\star/M_\odot) < 9.1$, from the NSA catalogue, leaving 4961 and then 480 galaxies, respectively. We also excluded systems more luminous than the Large Magellanic Cloud with an absolute magnitude cut of $M_g > -18.5$, which left 460 galaxies. These criteria are consistent with those of the MaNGA Dwarf Galaxy Sample (MaNDala; Cano-Díaz et al. 2022).

We then applied a spatial resolution cut, requiring $R_e \geq \theta_{PSF}$, where $\theta_{PSF} = 2.5''$ is the MaNGA point spread function full width at half maximum. This cut excludes spatially unresolved galaxies, whose gradients would be biased towards positive values by beam smearing (Acharyya et al. 2020). We show in Appendix A that even within the resolved sample a residual dependence of the measured gradient on R_e/θ_{PSF} persists, and we demonstrate that our main results are robust to applying a stricter cut of $R_e \geq 2\,\theta_{PSF}$. We also removed two galaxies with unphysical effective radii >50″ from failed photometric fits. These steps left 430 galaxies. We then ran the full stacking and emission line fitting pipeline on these galaxies and kept only those with at least three valid radial bins, which we defined by $S/N > 3$ in both Hα and [N II]. This removed 42 passive galaxies with no detectable emission and 6 galaxies with fewer than three valid bins. Our final sample contains 382 star-forming low-mass galaxies.

We applied the same selection criteria to the full DR17 sample rather than to a random subset. Our sample therefore includes essentially all MaNDala galaxies that pass our quality, resolution, and emission line cuts, along with many additional low-mass galaxies from the rest of the survey.

The final sample spans stellar masses of $7.2 \leq \log(M_\star/M_\odot) \leq 9.1$. The redshift selection criterion was $0.01 \leq z \leq 0.05$. Three galaxies in the final sample (11020−12701, 8554−12704, and 8150−3701) have catalogue redshifts below this limit, in the range $z = 0.0002$ to 0.0017, and were retained in error during the selection. We verified that these three galaxies passed all other quality, resolution, and emission-line criteria and had valid gradient measurements, and that their removal left the concentration correlation ($r = 0.304$), the median gradient slope (-0.007 dex R_e^{-1}), and the environmental null result unchanged. We therefore retained them. They were excluded from the $\Sigma_\star$ analysis in any case (Section 3.7), because peculiar velocities dominate the Hubble flow at these redshifts. In addition, for 23 galaxies we adopted Hα-derived redshifts (Section 3.2); these corrections were small and did not move any galaxy outside the selection range. The effective radii range from 2.5 to 32.7″, and R_e/θ_{PSF} ranges from 1.1 to 13.1. This is the largest spatially resolved spectroscopic sample of dwarf galaxies studied with MaNGA to date. For our comparative analysis, we split the sample at its median stellar mass, $\log(M_\star/M_\odot) = 8.89$, into a lower-mass group ($\log(M_\star/M_\odot) < 8.89$, $N = 191$) and a higher-mass group ($\log(M_\star/M_\odot) \geq 8.89$, $N = 191$). The low-mass end of our sample remains limited because MaNGA was not designed to target very low-mass galaxies, which is a fundamental limitation of the survey rather than of our selection. We show the sample characterisation in Figure 1 and list the complete properties in Table G.1.

Stellar masses were drawn from the NASA-Sloan Atlas (NSA; Blanton et al. 2011) and assumed a Chabrier (2003) initial mass function. We used the structural parameters, the effective radius, R_e, position angle, and axis ratio in the r band, to define the elliptical geometry of our radial binning. We took these parameters from the Sérsic profile analysis of DESI Legacy Survey imaging (Cano-Díaz et al. 2022) where available, and from the NSA catalogue and `drpall` file otherwise.

2.3. Ancillary catalogues

We made use of several ancillary catalogues to characterise the physical properties and environments of our sample galaxies. We derived integrated stellar population properties using the PIPE3D spectral fitting code (Sánchez et al. 2016). From PIPE3D we took the total star formation rate, the specific star formation rate, the luminosity- and mass-weighted stellar ages, the D4000 break strength, and the Hα equivalent width. We derived the star formation rate from the Hα emission line luminosity integrated over the full MaNGA field of view, using the Kennicutt (1998) conversion corrected to a Chabrier (2003) initial mass function. For galaxies without a PIPE3D measurement, we computed the star formation rate directly from the total Hα flux in the `EMLINE_GFLUX` extension of the DAP MAPS files. We integrated all unmasked spaxels with positive Hα flux, converted to luminosity at each galaxy's redshift, and applied the same calibration. The two approaches give consistent results. No dust correction was applied to the Hα fluxes used for star formation rate estimation.

We took morphological parameters from the MaNGA Visual Morphology Catalogue (Vázquez-Mata et al. 2022), which provides visual classifications and non-parametric measurements from DESI Legacy Survey imaging. From this catalogue we used light concentration, C, asymmetry, A, morphological T-type, an edge-on flag, and a tidal feature flag. The catalogue does not cover the full MaNGA sample, so concentration is available for 230 of our galaxies. Of these 230 galaxies, 219 pass the gradient quality cut ($\sigma_{\nabla\Delta Z} \leq 0.05$ dex R_e^{-1}) and are used in the correlation analysis. The remaining galaxies have no entry, which is a coverage limitation of the external catalogue rather than a quality cut on our part. We find that the galaxies with a measured concentration are statistically indistinguishable from those without in stellar mass, effective radius, redshift, star formation rate, and gradient slope (Mann-Whitney $p > 0.1$ in every case). The coverage fraction is also roughly uniform with stellar mass, so the concentration subsample is not significantly biased.

We drew large-scale environment parameters from the Galaxy Environment for MaNGA catalogue (GEMA; Argudo-Fernández et al. 2015), which characterises the surroundings of MaNGA galaxies in the SDSS spectroscopic survey. From this catalogue we used the number of neighbours within 1 and 5 Mpc, the group size, the group membership, the brightest group galaxy flag, the halo mass, and the isolation flag.

We measured the gas velocity dispersion from the `EMLINE_GSIGMA` extension of the DAP MAPS files (Westfall et al. 2019), which gives the Gaussian fit velocity dispersion of each emission line per spaxel. We adopted the median Hα velocity dispersion within $1\,R_e$ as our tracer of turbulent gas motions, which we denote as σ_{gas}. This is available for all our galaxies.

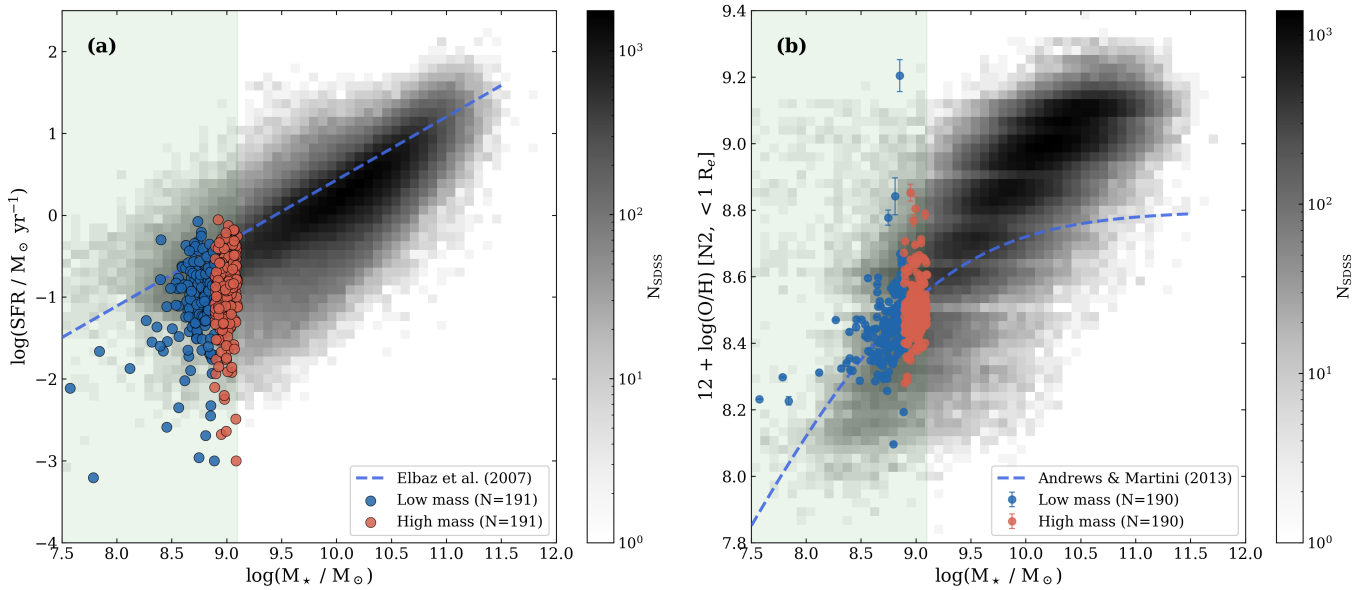


Fig. 1. Sample characterisation of the 382 dwarf galaxies used in this work. Left panel: Star-forming main sequence, with our galaxies colour coded by stellar mass group relative to the sample median ($\log(M_\star/M_\odot) = 8.89$). The grey histogram shows SDSS DR8 star-forming galaxies from the MPA-JHU catalogue, and the dashed line is the star-forming main sequence of Elbaz et al. (2007). Our galaxies lie systematically below this relation because it is calibrated for more massive galaxies; at low stellar masses, the relation has a lower normalisation at fixed stellar mass. Right panel: MZR, with our galaxies coloured by mass group over the SDSS star-forming population (grey), and the dashed line showing the MZR of Andrews & Martini (2013). The SDSS distribution and the Andrews & Martini (2013) relation are shown on their native abundance scales, which differ from the N2 calibration used for our galaxies. Because the N2 calibration saturates at a higher metallicity, our points and the SDSS distribution are not directly comparable in absolute abundance at the high-mass end; the comparison shows the location of our sample in the mass-metallicity plane rather than an exact abundance match. The right panel shows 190 galaxies per group rather than 191 because one galaxy (8934−9102) has an unphysically high N2 metallicity ($12 + \log(\mathrm{O/H}) = 9.20$) and is excluded from this panel but retained in the gradient analysis. The shaded green band marks the stellar mass range of our selection. SDSS background metallicities are central fibre values, while ours are inverse variance weighted means within 1 R_e.

3. Analysis pipeline

3.1. Continuum subtraction

Before fitting the emission lines, we subtracted the stellar continuum from each spaxel. We used the `STELLAR` extension of the LOGCUBE file, which is the best-fit stellar population model from the MaNGA Data Analysis Pipeline (Westfall et al. 2019), derived by fitting a linear combination of MILES stellar population templates (Sánchez-Blázquez et al. 2006) to the observed spectrum using penalised pixel fitting (pPXF; Cappellari 2017). This leaves a residual spectrum that contains only the emission line signal and noise,

$$F_{\mathrm{clean}}(\lambda, x, y) = F_{\mathrm{obs}}(\lambda, x, y) - F_{\mathrm{stellar}}(\lambda, x, y), \quad (1)$$

where F_{obs} is the observed flux from the `FLUX` extension. Figure 2 shows the observed maps for a representative galaxy.

3.2. Redshift estimation

We adopted the systemic redshift of each galaxy from the NSA catalogue. As a consistency check, we also measured the redshift from the observed peak wavelength of Hα in the central-bin stacked spectrum, which is the strongest line in our spectra. For the large majority of galaxies, the two values agree to within the noise, and we retain the NSA redshift. For 23 galaxies the Hα-derived redshift differs from the NSA value by more than 100 km s^{-1}, and we adopted the Hα redshift instead, as it was measured directly from the spectral data. For 22 of these galaxies, the velocity difference is between 100 and 130 km s^{-1}, consistent with small systematic offsets in the NSA photometric redshifts at a low redshift. One galaxy (8719−9101) shows a larger discrepancy of 2754 km s^{-1}, which we attribute to an incorrect NSA redshift assignment, likely from a brighter neighbouring object. For this galaxy the emission-line fitting was performed within a ±400 km s^{-1} window centred on the NSA redshift, so the measured gradient reflects the spectral features at that redshift position regardless of the adopted systemic value. The gradient measurement for this galaxy should therefore be treated with caution. In all cases the emission line measurements themselves are unaffected by this correction, as the redshift enters only through the rest-frame wavelength calibration and not through the flux or signal-to-noise of the stacked spectra. As a result of these corrections, a small number of galaxies in the final sample have adopted redshifts below the nominal lower limit of $z = 0.01$. The adopted redshift defines the rest-frame wavelength array, $\lambda_{\mathrm{rest}} = \lambda_{\mathrm{obs}}/(1 + z)$, that we used to fit all four emission lines.

3.3. Spatial geometry and elliptical binning

For each galaxy we defined elliptical radial bins using the position angle and axis ratio described in Section 2.2. The elliptical radius of each spaxel is

$$r_{\mathrm{ellip}} = \sqrt{x_{\mathrm{rot}}^2 + \left(\frac{y_{\mathrm{rot}}}{b/a}\right)^2} \times 0.5'', \quad (2)$$

where x_{rot} and y_{rot} are the spaxel co-ordinates rotated to align with the major axis, b/a is the axis ratio, and the factor 0.5″

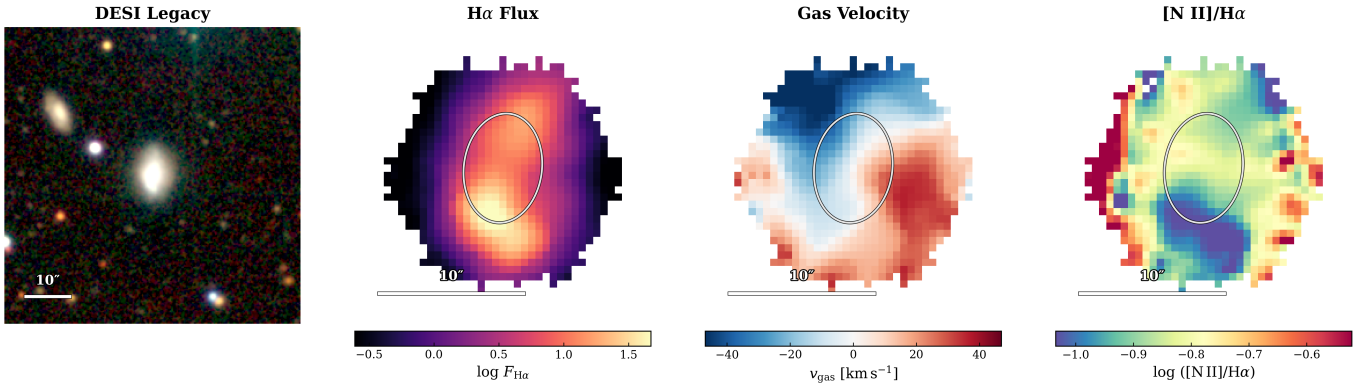


Fig. 2. Representative galaxy in our sample (MaNGA `Plate-IFU`: 8563–3704, $\log(M_\star/M_\odot) = 8.63$). From left to right: DESI Legacy Survey RGB image, Hα flux, gas velocity field, and [N II]/Hα ratio, which is the N2 metallicity calibrator. The 1 R_e ellipse is marked on the map panels and 10″ scale bars are shown. The velocity and [N II]/Hα maps are restricted to spaxels with Hα $S/N > 3$.

converts spaxels to arcseconds. The rotation is

$$x_{\rm rot} = x\cos\phi + y\sin\phi, \qquad y_{\rm rot} = -x\sin\phi + y\cos\phi, \tag{3}$$

where $\phi = \phi_{\rm PA} - 90°$. Here $\phi_{\rm PA}$ is the galaxy position angle from the structural parameters (Section 2.2), which we converted to the mathematical convention. We normalised the radius as $r_{\rm norm} = r_{\rm ellip}/R_e$.

We defined ten annular bins of width $0.2\,R_e$ from 0 to $2.0\,R_e$, with centres at $0.1, 0.3, \ldots, 1.9\,R_e$. Figure 3 shows the binning scheme, the resulting metallicity map, and the radial profiles for a representative galaxy.

When we computed median radial profiles, we took the median at each bin centre over only those galaxies with a valid measurement at that radius. The outer bins of the median profile therefore rest on fewer galaxies than the inner bins, and are correspondingly less certain in Figure 4.

3.4. Spectral stacking

Within each bin we combined the continuum subtracted spectra of all valid spaxels using an inverse variance weighted mean,

$$F_{\rm stack}(\lambda) = \frac{\sum_i F_i(\lambda)\, w_i(\lambda)}{\sum_i w_i(\lambda)}, \tag{4}$$

where $w_i(\lambda) = \sigma_i^{-2}(\lambda)$ is the inverse variance weight from the `IVAR` extension. We included only spaxels with `MASK` = 0 near Hα, and we discarded bins with fewer than three valid spaxels. We propagated the stacked inverse variance, $w_{\rm stack}(\lambda) = \sum_i w_i(\lambda)$, into the line flux uncertainties.

3.5. Emission line fitting

We fitted each stacked spectrum with two simultaneous multi-component Gaussian models: one for the Hα + [N II] complex and one for the Hβ + [O III] complex (Belfiore et al. 2017).

For the Hα + [N II] complex, we fitted Hα (6562.8 Å), [N II]λ6583 (6583.4 Å), and [N II]λ6548 (6548.1 Å). All three components share one velocity offset and width σ, and we fixed the [N II]λ6548/λ6583 = 1/3 ratio at its theoretical value (Storey & Zeippen 2000), since the two lines share the same upper energy level. This leaves four free parameters: the two amplitudes, the offset, and σ. We constrained the offset to $\pm 400\,{\rm km\,s^{-1}}$ and σ to 0.5 to 8.0 Å. We fitted the Hβ + [O III] complex in the same way for Hβ (4861.3 Å), [O III]λ5007 (5006.8 Å), and [O III]λ4959 (4958.9 Å), fixing the [O III]λ4959/λ5007 = 1/2.98 ratio (Storey & Zeippen 2000) and using the same offset and σ constraints.

We retained a bin only if both fits converged, σ lay within bounds, all amplitudes were positive, and $S/N \geq 3$ in both Hα and [N II]λ6583. The N2 calibration depends only on these two lines, so we imposed no S/N requirement on Hβ or [O III]λ5007 for the bins used in N2. Where we also computed the O3N2 calibration, we additionally required $S/N \geq 3$ in both of those lines. This relaxed N2 criterion recovers additional valid bins in the low-surface-brightness outer regions, where Hβ and [O III] are too faint to detect. We define the signal-to-noise ratio as

$$S/N = \frac{F_{\rm line}}{\sigma_F}, \tag{5}$$

where the flux error is

$$\sigma_F = \sqrt{\sum_j w_{\rm stack}^{-1}(\lambda_j)} \cdot \sigma \cdot \sqrt{2\pi}, \tag{6}$$

summed over pixels within 3σ of the line centre, where σ is the fitted Gaussian width in ångström.

3.6. Metallicity calibration

We derived the gas-phase metallicity using the strong line calibrations of Pettini & Pagel (2004). Throughout this paper we use the symbol Z as a shorthand for the logarithmic oxygen abundance 12 + log(O/H), not the total metal mass fraction. Our primary indicator is the N2 index,

$$12 + \log({\rm O/H}) = 8.90 + 0.57 \times \log\left(\frac{[{\rm N\,II}]\lambda6583}{{\rm H}\alpha}\right). \tag{7}$$

We also use the O3N2 index of Pettini & Pagel (2004) to check how much our results change relative to the N2 calibration. We define it as

$${\rm O3N2} = \log\left(\frac{[{\rm O\,III}]\lambda5007/{\rm H}\beta}{[{\rm N\,II}]\lambda6583/{\rm H}\alpha}\right), \tag{8}$$

which gives

$$12 + \log({\rm O/H}) = 8.73 - 0.32 \times {\rm O3N2}. \tag{9}$$

We adopt N2 as our primary calibration for two reasons. First, it uses only Hα and [N II], which are closely spaced in wavelength

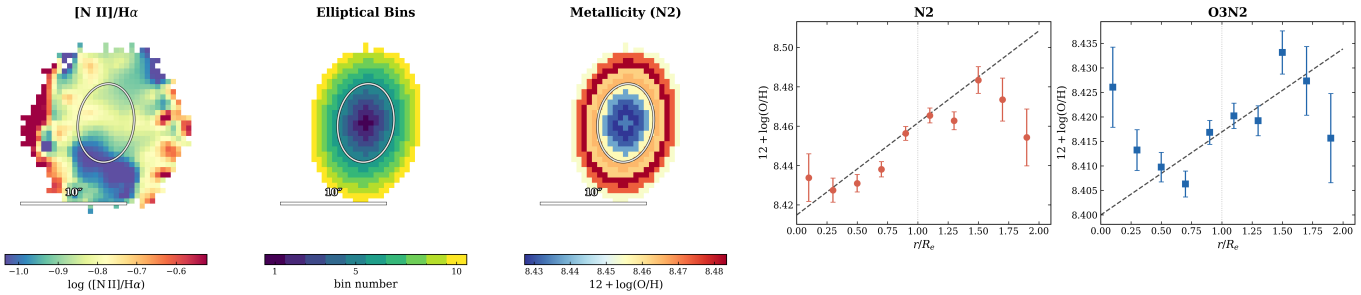


Fig. 3. Analysis sequence for the representative galaxy 8563−3704. From left to right: [N II]/Hα ratio map, elliptical binning map (0.2 R_e bins to 2 R_e), two-dimensional N2 metallicity map, and the radial metallicity profiles derived using the N2 (fourth panel) and O3N2 (fifth panel) calibrations of Pettini & Pagel (2004). Placing the [N II]/Hα map beside the N2 metallicity map shows directly how the line ratio translates into 12 + log(O/H). For this galaxy the N2 and O3N2 profiles yield consistent radial slopes; a statistical comparison of both calibrations across the full sample is presented in Appendix F.

and so insensitive to differential extinction and flux calibration uncertainties (Pettini & Pagel 2004). We can also measure N2 in the outer low-surface-brightness bins, where Hβ and [O III] are undetected. Second, we show in Figure 3 that adopting O3N2 instead leaves the shape and slope of the radial metallicity gradient essentially unchanged for the representative galaxy shown. A full statistical comparison of both calibrations across the sample is presented in Appendix F. N2 is also widely used in the literature, which makes it straightforward to compare our gradients with previous work.

We propagated the metallicity uncertainties analytically from the line flux errors. For N2,

$$\sigma_{Z,N2} = \frac{0.57}{\ln 10}\sqrt{\left(\frac{\sigma_{NII}}{F_{NII}}\right)^2 + \left(\frac{\sigma_{H\alpha}}{F_{H\alpha}}\right)^2}, \tag{10}$$

and for O3N2,

$$\sigma_{Z,O3N2} = \frac{0.32}{\ln 10}\sqrt{\sum_X \left(\frac{\sigma_X}{F_X}\right)^2}, \tag{11}$$

summed over $X \in \{[O\,III]\,\lambda5007, H\beta, [N\,II]\lambda6583, H\alpha\}$.

3.7. Stellar mass surface density

For each galaxy we computed the stellar mass surface density, $\Sigma_\star$, per spaxel. We integrated the best-fit stellar continuum (STELLAR) over the rest-frame range 5000 to 7000 Å to obtain a luminosity proxy map, which we normalised by the total integrated luminosity to give each spaxel's fractional contribution to the stellar light,

$$\Sigma_\star(x,y) = M_\star \times \frac{L(x,y)}{L_{total}} \times \frac{1}{A_{spaxel}}, \tag{12}$$

where $M_\star$ is the total stellar mass from the NSA catalogue, $L(x,y)/L_{total}$ is the fractional contribution of each spaxel to the integrated stellar light, and A_{spaxel} is the physical area per spaxel in square kiloparsecs. This approach assumes a spatially constant mass-to-light ratio across all spaxels. While per-spaxel stellar mass maps from full spectral fitting would provide a more direct estimate of $\Sigma_\star$, we expect this approximation to have a minor effect on our results, since low-mass star-forming galaxies tend to have relatively uniform stellar populations across their discs, limiting the magnitude of any radial mass-to-light ratio gradient. We computed A_{spaxel} from the angular diameter distance, assuming a flat Λ cold dark matter cosmology ($H_0 = 70\,km\,s^{-1}\,Mpc^{-1}$, $\Omega_M = 0.3$, $\Omega_\Lambda = 0.7$). The resulting $\Sigma_\star$ is expressed in solar masses per square kiloparsec, and we use $\log(\Sigma_\star)$ throughout. For each radial bin, we adopted the median $\Sigma_\star$ as its representative value. We excluded three galaxies with $z < 0.002$ here, because peculiar velocities dominate over the Hubble flow at such low redshifts and make the angular diameter distance, and hence A_{spaxel}, unreliable (Blanton et al. 2005). This leaves 379 galaxies with $\Sigma_\star$.

3.8. Residual metallicity

The metallicity of a galaxy depends primarily on its stellar mass, which is traced locally by the stellar mass surface density, $\Sigma_\star$. We want to subtract out this primary dependence and recover any secondary dependencies on other physical parameters. We therefore define a residual metallicity, ΔZ, by subtracting from each bin the value predicted by a global linear fit between metallicity and $\log(\Sigma_\star)$ across all valid bins, performed using ordinary least squares without weighting by individual measurement uncertainties, treating each bin as an independent data point,

$$\Delta Z = Z_{N2} - Z_{pred}(\Sigma_\star), \tag{13}$$

where $Z_{pred}(\Sigma_\star) = 0.0963 \times \log(\Sigma_\star) + 7.7643$. We fitted this relation across all 3608 valid bins from the full sample (Pearson $r = 0.371$, $p = 2.0 \times 10^{-118}$), and we show it in Figure C.1 in Appendix C. We also subtracted a small systematic radial trend of $+0.017\,dex\,R_e^{-1}$ from the residual profiles to account for the non-zero mean gradient introduced by the linear approximation to the Z–$\Sigma_\star$ relation; we demonstrate in Appendix B that this correction leaves all correlation results unchanged. A positive ΔZ means a bin is more metal-rich than its local stellar mass surface density predicts, and a negative value means it is more metal-poor.

3.9. Gradient slope fitting

For each galaxy we measured two gradient slopes by fitting straight lines to its radial profiles with weighted least squares (χ^2 minimisation), weighting each bin by the inverse variance of its metallicity. Fitting Z_{N2} against the normalised radius, r/R_e, gives the metallicity gradient, ∇Z, and fitting the residual metallicity, ΔZ, in the same way gives the residual metallicity gradient, $\nabla\Delta Z$. Both slopes are expressed in dex per effective radius. We adopted the scaled slope uncertainty, which inflates the formal error by the residual scatter about the fit and so accounts

for intrinsic profile scatter beyond the measurement errors. We included only galaxies with at least three valid bins.

For the correlation analysis (Section 4), we further restricted the analysis to a clean sample of 366 galaxies with a well-constrained gradient slope, $\sigma_{\nabla\Delta Z} \leq 0.05\,\mathrm{dex}\,R_\mathrm{e}^{-1}$. We set this threshold by fit quality rather than by any outcome. It removes only 13 of 379 galaxies, and the excluded objects are demonstrably poorly constrained. They have a median of six valid radial bins, against ten for the retained sample, and a median slope uncertainty of $0.063\,\mathrm{dex}\,R_\mathrm{e}^{-1}$, against 0.009 for the clean sample. The cut therefore isolates unreliable, often non-linear profiles, including several confirmed mergers, independently of any correlation.

3.10. Visual environmental classification

To complement the GEMA environment parameters (Section 2.3), we visually classified all our galaxies using DESI Legacy Survey DR10 colour images from the Legacy Survey viewer. For each galaxy we downloaded a cutout large enough to include the MaNGA field of view and its immediate surroundings, typically 60−120″ on a side depending on the galaxy size, and generated an RGB image from the g, r, and z bands with an arcsinh stretch (Lupton et al. 2004). We placed each galaxy into one of two classes. We classified a galaxy as isolated when it showed no companions, tidal features, or signs of interaction in the field or wider surroundings. We classified it as disturbed when it showed clear interaction signatures, such as close companions, tidal tails, asymmetric morphology, or a companion overlapping the integral field unit footprint.

The light concentration, C, and asymmetry, A, used in our analysis were taken from the MaNGA Visual Morphology Catalogue (Vázquez-Mata et al. 2022) and were measured from DESI Legacy Survey r-band imaging. Concentration is defined as $C = 5\log(r_{80}/r_{20})$, where r_{80} and r_{20} are the radii enclosing 80 and 20 percent of the total flux within the Petrosian ellipse (Conselice 2003). Asymmetry is defined as $A = \sum |I - I_{180}| / \sum |I|$, where I_{180} is the galaxy image rotated by 180° about its centre (Abraham et al. 1996).

This classification yielded 182 isolated and 200 disturbed galaxies. As an independent check, we compared the asymmetry of the two classes. Disturbed galaxies have a higher mean asymmetry ($A = 0.291$) than isolated galaxies ($A = 0.180$), and the difference is significant (Mann-Whitney $p = 10^{-4}$), which validates the classification. We recorded the classification flag in the master catalogue and used it in the environmental analysis (Section 4.3).

4. Results

4.1. Sample characterisation

Our final sample lies on the star-forming main sequence, which confirms that these are actively star-forming systems (Figure 1, left panel). The galaxies follow the low-mass extension of the relation of Elbaz et al. (2007), though with a systematic offset towards lower star formation rates at a fixed stellar mass, as expected for the low-mass regime (Section 2.3). The right panel shows the MZR from the N2 calibration. We compare it to the SDSS DR8 background from the MPA-JHU catalogue and to the reference relation of Andrews & Martini (2013), noting that the SDSS distribution and the literature relation are shown on their native abundance scales, which differ from our N2 calibration and are therefore not directly comparable in absolute metallicity. Our sample shows a significant positive correlation between stellar mass and gas-phase metallicity (Pearson $r = 0.444$, $r^2 = 0.197$, $p < 0.001$), though stellar mass accounts for only 20 percent of the observed variance in metallicity, indicating that other processes also contribute to the scatter. The SDSS background metallicities are single 3″ fibre values, which represent roughly the central metallicity of each galaxy. Ours are inverse variance weighted means within $1\,R_\mathrm{e}$, which for galaxies with negative gradients lie slightly below the central value.

4.2. Metallicity and residual metallicity gradients

The left panel of Figure 4 shows the radial metallicity profiles of our galaxies, with individual profiles in the background and median profiles for the low- and high-mass groups. We split the groups at the sample median $\log(M_\star/M_\odot) = 8.89$. We find that metallicity gradients are flat on average, with a median slope of $-0.007\,\mathrm{dex}\,R_\mathrm{e}^{-1}$ and a standard deviation of $0.071\,\mathrm{dex}\,R_\mathrm{e}^{-1}$. The distribution is strongly peaked about zero. Most galaxies (87 percent) have slopes within $\pm 0.1\,\mathrm{dex}\,R_\mathrm{e}^{-1}$, and only a few outliers reach $|\nabla Z| \gtrsim 0.2\,\mathrm{dex}\,R_\mathrm{e}^{-1}$. This near-zero distribution is broadly consistent with efficient metal mixing in shallow gravitational potential wells (Mercado et al. 2021), though we note that beam smearing may contribute to the observed flattening in the less well resolved galaxies; we demonstrate in Appendix A that the median slope becomes more negative ($-0.026\,\mathrm{dex}\,R_\mathrm{e}^{-1}$) when a stricter resolution cut is applied. Both mass groups have equally flat gradients, but the high-mass group lies at higher metallicity than the low-mass group at every radius. The two groups therefore differ in their overall metallicity but not in the shape of their gradients. More massive galaxies are uniformly more metal-rich, while the way metallicity changes with radius is similar regardless of mass.

We quote two complementary measures of the gradient. The median slope above, $-0.007\,\mathrm{dex}\,R_\mathrm{e}^{-1}$, comes from fitting a straight line to each galaxy individually and taking the median of the resulting per-galaxy slopes. This is a property of the galaxy population and has a well-defined distribution (standard deviation $0.071\,\mathrm{dex}\,R_\mathrm{e}^{-1}$), and it is the quantity we use throughout our correlation analysis (Section 4.3). The straight lines drawn in Figure 4 are different. We fit them to the binned median profile of each group, that is, to the stacked medians rather than to individual galaxies, and they have a slightly steeper slope ($-0.016\,\mathrm{dex}\,R_\mathrm{e}^{-1}$ for the full sample). Both measures describe flat gradients. We adopt the per-galaxy median as our primary measurement because it retains the galaxy-to-galaxy distribution we need for the statistical analysis, and we use the binned-median fit only to guide the eye in the figure.

We find a statistically significant positive correlation between the gas-phase metallicity and local stellar mass surface density across all valid bins ($Z = 0.0963 \times \log(\Sigma_\star) + 7.7643$, Pearson $r = 0.371$, $r^2 = 0.138$, and $p = 2.0 \times 10^{-118}$), indicating that denser regions are on average more metal-rich, though the local stellar mass surface density accounts for only 14 percent of the observed variance in metallicity. This relation holds across all radii and is not driven by any single radial zone. The two mass groups remain offset in metallicity even at fixed $\Sigma_\star$. This shows that total stellar mass affects metallicity independently of local density, and motivates the residual metallicity ΔZ that we define in Section 3.8.

The right panel of Figure 4 shows the ΔZ profiles, computed by removing the $\Sigma_\star$ dependence as described in Section 3.8. A clear mass offset remains. The high-mass group sits systematically above $\Delta Z = 0$ at most radii, while the low-mass group sits

below. This suggests that total stellar mass has an independent effect on chemical enrichment beyond what local stellar density predicts, and the offset persists at all radii.

4.3. Drivers of the metallicity gradient

We now look for the physical properties that drive the galaxy-to-galaxy diversity in the metallicity gradient. Our main test is the correlation between each property and the residual gradient slope, $\nabla\Delta Z$, which is the slope of a straight-line fit to the residual metallicity, ΔZ, against r/R_e (Sections 3.8 and 3.9). Since ΔZ already has the primary mass dependence removed, a correlation with $\nabla\Delta Z$ isolates the effect of each property on the radial metallicity structure, independent of stellar mass. We test the stellar mass, star formation rate, gas velocity dispersion, light concentration, asymmetry, and the large scale environment from visual classification and the GEMA catalogue. We report both Pearson and Spearman correlation coefficients throughout, and we treat a correlation as significant when $p < 0.05$ in both tests. We also report the coefficient of determination, r^2, which gives the fraction of variance in $\nabla\Delta Z$ explained by each property, as a measure of the effect size.

We present four of these properties, light concentration, gas velocity dispersion, star formation rate, and environment, in the three-panel figures (Figures 5–8). The three panels are the same in each figure. We split the sample at the median of the property into a higher and a lower group, shown throughout in contrasting colours. For light concentration the measurement is available for only 230 galaxies, so its panels use two mass bins rather than the three used for the other properties. The left panel shows the inner metallicity $Z(1\,R_e)$ against stellar mass, where $Z(1\,R_e)$ is the inverse variance weighted mean N2 metallicity over all bins within $1\,R_e$. This panel recovers the MZR and shows whether the overall metallicity level depends on the property. The middle panel shows the raw gradient slope, ∇Z, against stellar mass. A positive value means that metallicity rises outwards and a negative value means that it falls outwards, so this panel shows whether the property makes the gradient flatter, steeper, or inverted. The right panel shows the median residual profiles, $\Delta Z(r)$, for the two groups. A separation between the two groups here means that the property shapes the radial metallicity structure independently of mass.

The correlation analysis uses a clean sample of 366 galaxies. We obtained it from the full sample of 382 by removing three galaxies at $z < 0.002$, for which ΔZ could not be computed, and thirteen with poorly constrained gradient slopes ($\sigma_{\nabla\Delta Z} > 0.05\,\mathrm{dex}\,R_e^{-1}$), which are noisy or non-linear profiles including several confirmed mergers. Concentration is the only property not measured for essentially the full sample, being available for 230 galaxies. For the middle panels, we ran a complementary test on the raw slope ∇Z using mass-matched subsamples. We matched following Wisz et al. (2025), randomly discarding galaxies from the larger group in each mass bin until the two groups had an identical mass distribution. Any remaining difference between them reflects the property, then, rather than a residual dependence on mass. Table 1 collects the correlation coefficients for each property.

Light concentration, C, shows the strongest and most significant correlation with the residual gradient (Pearson $r = 0.304$, Spearman $r = 0.241$, $r^2 = 0.092$, $p < 0.001$; Figure 5), though it accounts for only 9 percent of the observed variance in $\nabla\Delta Z$. Monte Carlo error propagation confirms that this result is robust to measurement uncertainties in the gradient slopes, with a 68 percent confidence interval of $r \in [0.283, 0.313]$ (Appendix E). The high-concentration galaxies have a more positive residual gradient than the low-concentration galaxies, with median $\nabla\Delta Z = +0.043$ against $+0.013\,\mathrm{dex}\,R_e^{-1}$. Their residual profiles show the clearest separation of any property we test, with the high-concentration group rising from $\Delta Z = -0.064$ at $0.1\,R_e$ to -0.026 on the outskirts, while the low-concentration group rises from -0.027 to $+0.014$, suggesting that the centres of concentrated galaxies tend to be metal- poor relative to what their high local stellar density predicts. The concentration result persists when a stricter resolution cut is applied ($R_e \geq 2\,\theta_{PSF}$, $r = 0.234$, $p = 0.006$; Appendix A), though the effect size is reduced.

Gas velocity dispersion, σ_{gas}, shows a statistically significant correlation with the residual gradient (Pearson $r = 0.204$, Spearman $r = 0.289$, $r^2 = 0.041$, $p < 0.001$; Figure 6), with high-dispersion galaxies tending to have more positive residual gradients. We note that σ_{gas} as measured from the MaNGA data shows some dependence on spatial resolution, suggesting that beam smearing may contribute to the measured dispersion in poorly resolved galaxies. The correlation with $\nabla\Delta Z$ should therefore be interpreted with some caution, and we return to this in Section 5.3.

The star formation rate shows a marginal but significant correlation in both Pearson and Spearman tests (Pearson $r = 0.106$, $p = 0.042$; Spearman $r = 0.138$, $p = 0.008$; $r^2 = 0.011$; Figure 7), most likely through its link to stellar mass (Section 5.5). The star formation rate accounts for only 1 percent of the variance in $\nabla\Delta Z$, and we regard this as a weak and tentative association. The total stellar mass shows no significant Pearson correlation with the residual gradient ($r_P = -0.078$, $p = 0.134$), though the Spearman test gives a marginally significant result ($r_S = -0.116$, $p = 0.027$), suggesting a weak rank correlation that is not well described by a linear model.

The large-scale environment has no detectable effect. Disturbed and isolated galaxies (Figure 8) differ neither in gradient slope ($r = 0.006$, $p = 0.914$) nor in their residual profiles, which overlap at all radii. This is a robust null result across both Pearson and Spearman tests and across all environment indicators from the GEMA catalogue, indicating that the large-scale environment does not measurably influence the radial distribution of metals in our sample. Figure 9 summarises the full set of coefficients, and we discuss the physical interpretation in Section 5.

5. Discussion

5.1. Flat metallicity gradients in low-mass galaxies

We find that the metallicity gradients across our low-mass MaNGA galaxies are flat on average (Figure 4, Section 4.2). The median slope is $-0.007\,\mathrm{dex}\,R_e^{-1}$, with a galaxy-to-galaxy scatter of $0.071\,\mathrm{dex}\,R_e^{-1}$. We note that beam smearing in the less well- resolved galaxies may contribute to this flattening; when a stricter resolution cut of $R_e \geq 2\,\theta_{PSF}$ is applied, the median slope shifts to $-0.026\,\mathrm{dex}\,R_e^{-1}$ (Appendix A), which may be a closer approximation to the intrinsic population median. In either case the slopes are distributed broadly about zero, consistent with a balance between mild negative and mild positive gradients rather than uniformly flat profiles.

This behaviour differs from that of massive spiral galaxies, in which inside-out disc growth produces clearly negative gradients (Sánchez et al. 2014; Belfiore et al. 2017). Our low-mass galaxies instead show flat and broadly scattered gradients, with no strong preference for a negative slope. Our results extend the gradient flattening that Belfiore et al. (2017) saw towards the low-mass end of MaNGA to a homogeneous sample that reaches well

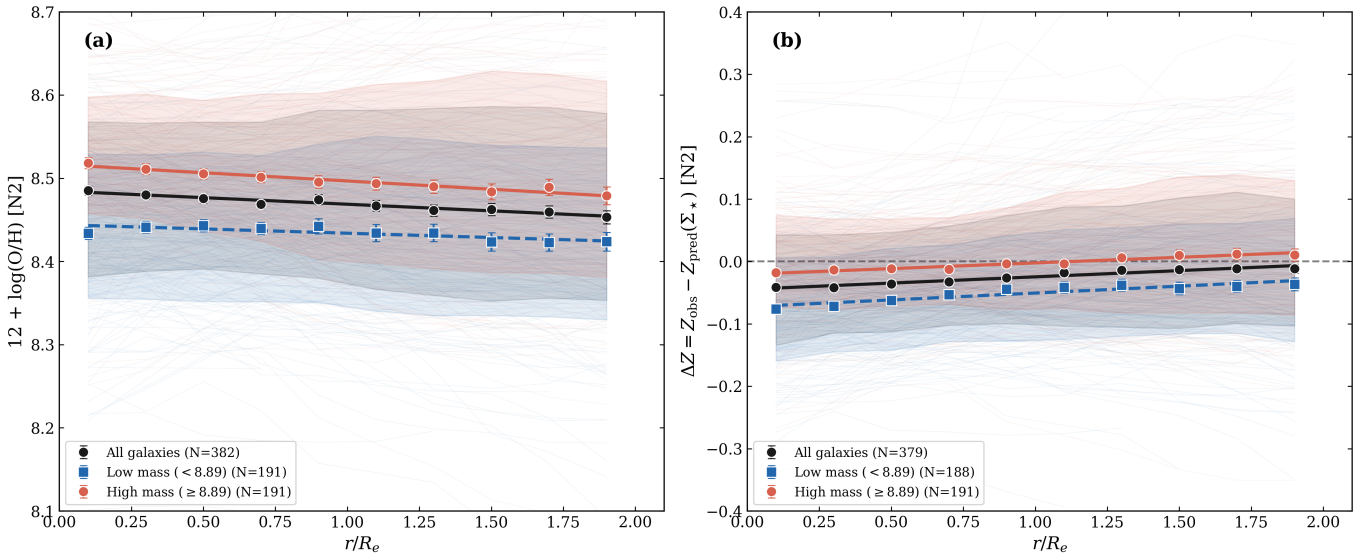


Fig. 4. Left: Radial gas-phase metallicity profiles for all 382 galaxies. Faint coloured lines are individual galaxies; markers show the median metallicity per radial bin for the higher mass ($\log(M_\star/M_\odot) \geq 8.89$, red) and lower-mass (<8.89, blue) groups, split at the sample median, with error bars giving the standard error, $\sigma/\sqrt{N}$, and shading the 16th to 84th percentile range. The solid and dashed straight lines are linear fits to the binned medians of the higher- and lower- mass groups, respectively. Right: Residual metallicity, $\Delta Z = Z_{\rm obs} - Z_{\rm pred}(\Sigma_\star)$, profiles for the same groups. Three galaxies with $z < 0.002$ are excluded from this panel because their $\Sigma_\star$ measurement is unreliable at such low redshifts (Section 3.7); symbols, errors, and fit lines as in the left panel. The horizontal dashed line marks $\Delta Z = 0$. The fit to the binned median profile is nearly flat in metallicity (slope $-0.016\,\mathrm{dex}\,R_{\rm e}^{-1}$ for the full sample) and rises gently in the residual ($+0.020\,\mathrm{dex}\,R_{\rm e}^{-1}$); these describe the plotted median trend and differ from the median of the per-galaxy gradient slopes quoted in the text. The higher-mass group lies systematically above the lower-mass group in both panels.

Table 1. Correlation coefficients between each physical property and the residual gradient slope, $\nabla\Delta Z$.

Property	r_P	r_S	r^2	p_P	p_S	$r(\nabla Z)$
Concentration	+0.304	+0.241	0.092	<0.001	<0.001	+0.217
Gas vel. disp.	+0.204	+0.289	0.041	<0.001	<0.001	+0.184
SFR	+0.106	+0.138	0.011	0.042	0.008	+0.060
Environment	+0.006	−0.026	0.000	0.914	0.617	−0.005
Stellar mass	−0.078	−0.116	0.006	0.134	0.027	...

Notes. Computed over the clean sample of 366 galaxies, except for concentration, which uses the 219 galaxies with both a valid concentration measurement and a well-constrained gradient slope. r_P and r_S are the Pearson and Spearman correlation coefficients, r^2 the coefficient of determination, and p_P and p_S the corresponding p values. The $r(\nabla Z)$ column gives the complementary raw-gradient Pearson correlation on mass-matched subsamples. Stellar mass has no $r(\nabla Z)$ entry because mass-matching is not applicable when splitting by stellar mass itself.

into the dwarf galaxy regime, consistent with recent dedicated studies of the dwarf regime (Li et al. 2025; Valé et al. 2025).

A small number of galaxies stand out with strongly positive, inverted gradients. Roughly 11 of our 382 galaxies (3 per cent) have $\nabla Z > 0.15\,\mathrm{dex}\,R_{\rm e}^{-1}$, and the most extreme reaches $+0.28\,\mathrm{dex}\,R_{\rm e}^{-1}$. Positive gradients of this magnitude have been reported in other low-mass samples and attributed to the inflow of metal-poor gas to the central regions (Grossi et al. 2020), though we do not find a statistically significant association between positive gradients and disturbed morphology in our sample (Section 4.3). Alternative explanations, including residual beam-smearing effects or stochastic star formation histories, cannot be excluded.

5.2. Concentration as a driver of metallicity gradients

Light concentration, C, shows the most significant association with the metallicity gradient, both in the raw gradient slope, ∇Z (middle panel of Figure 5), and in the stellar-mass-subtracted residual slope, $\nabla\Delta Z$ (right panel). We split the sample at the median, $C = 2.909$. The left panel shows that the high- and low-C groups follow the same MZR, so the overall metallicity level does not vary with concentration. The middle panel shows that the high-C group tends to have more positive raw slopes ($r = 0.217$, $p = 0.002$). The right panel shows the same trend in the residual (Pearson $r = 0.304$, Spearman $r = 0.241$, $r^2 = 0.092$, $p < 0.001$), though concentration accounts for only 9 percent of the variance in $\nabla\Delta Z$. Monte Carlo error propagation gives a 68 percent confidence interval of $r \in [0.283, 0.313]$ (Appendix E), confirming the result is stable to measurement uncertainties. The high-C group has a median residual slope of $\nabla\Delta Z = +0.043$ against $+0.013\,\mathrm{dex}\,R_{\rm e}^{-1}$ for the low-C group. The raw and residual correlations agree, suggesting the trend is not an artefact of the mass subtraction.

We note that the two median residual profiles in the right panel of Figure 5 differ primarily in normalisation rather than slope, with the high-C group rising from $\Delta Z = -0.064$ at $0.1\,R_{\rm e}$

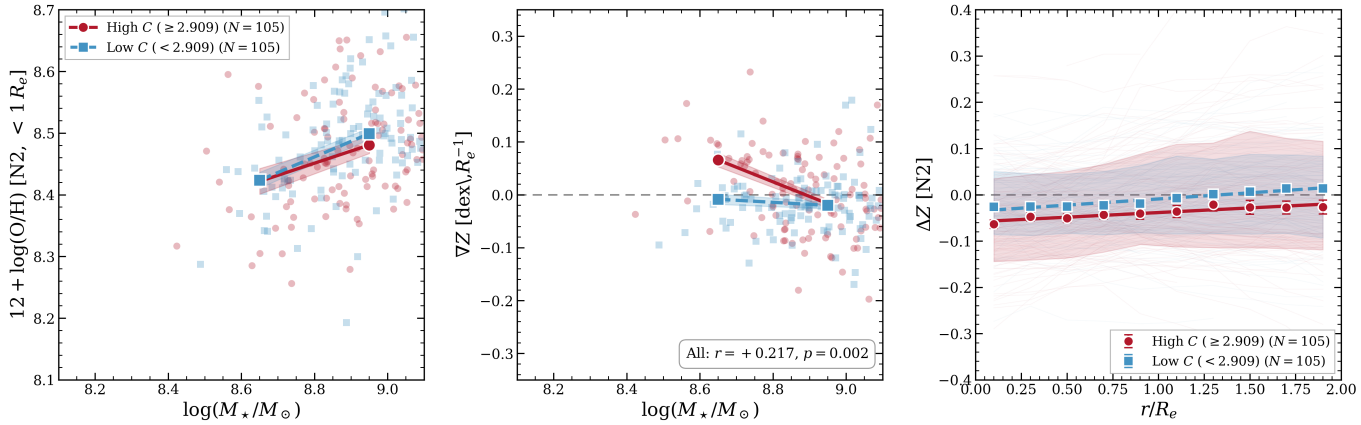


Fig. 5. Dependence of gas-phase metallicity on light concentration, C, split at the median $C = 2.909$ into high-C (red circles, solid) and low-C (blue squares, dashed) mass-matched subsamples. Left: Inner metallicity, $Z(1\,R_e)$, the inverse variance weighted mean N2 metallicity within $1\,R_e$ (Section 4.3), against stellar mass. Small markers are individual galaxies and large connected markers are the median trend in 0.3 dex mass bins with standard errors. This panel recovers the MZR and shows whether the overall metallicity level depends on concentration. Centre: Raw gradient slope, ∇Z (Section 3.9), from a straight-line fit to Z_{N2} against r/R_e, against stellar mass. The dashed line marks a flat gradient, and the annotation gives the Pearson correlation between C and ∇Z on the mass-matched subsamples. Right: Radial profiles of the residual metallicity, $\Delta Z = Z_{\mathrm{obs}} - Z_{\mathrm{pred}}(\Sigma_\star)$ (Section 3.8). Faint lines are individual galaxies, and bold markers are the median per group with standard errors and a 16th to 84th percentile band. The dashed line marks $\Delta Z = 0$. The high-concentration subsample shows the clearest separation of residual profiles of any property we test.

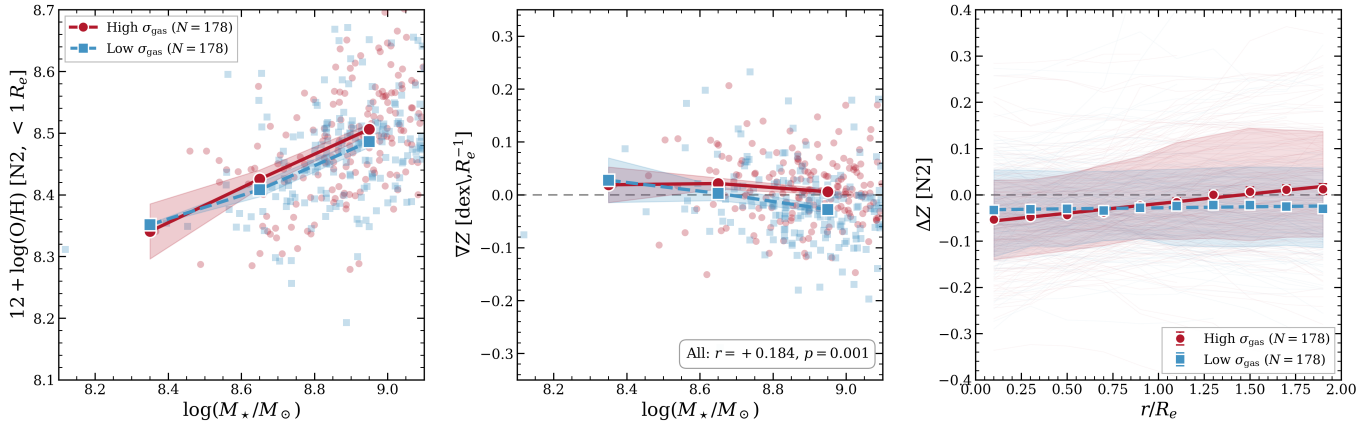


Fig. 6. As Figure 5, but split at the median gas velocity dispersion $\sigma_{\mathrm{gas}} = 72.5\,\mathrm{km\,s^{-1}}$ into high-σ_{gas} (red circles, solid) and low-σ_{gas} (blue squares, dashed) mass-matched subsamples. The left panel shows little dependence of the overall metallicity level on σ_{gas}. The centre panel shows a positive correlation between σ_{gas} and the raw gradient slope on the mass-matched subsamples ($r = +0.184$, $p = 0.001$). The right panel shows that the residual profiles of the high-dispersion subsample lie systematically above those of the low-dispersion subsample. We note that σ_{gas} shows some dependence on spatial resolution and the result should be interpreted with caution.

to -0.026 on the outskirts and the low-C group rising from -0.027 to $+0.014$. This is expected: stacking many galaxies averages out the individual gradient differences, so the separation between the group median profiles reflects the difference in median ΔZ level rather than the difference in median slope. The per-galaxy slope distribution, which is the quantity entering the correlation analysis, captures this slope difference directly. The result persists when a stricter PSF resolution cut is applied, though with a reduced effect size ($R_e \geq 2\,\theta_{\mathrm{PSF}}$, $r = 0.234$, $p = 0.006$; Appendix A).

A positive residual gradient means the centre is metal-poor relative to what its high local stellar mass surface density predicts. In concentrated galaxies the central stellar density is high, so the Z–$\Sigma_\star$ relation predicts a high central metallicity, yet the measured central gas-phase metallicity falls below it. The stars in the centre are metal-rich, as their high density implies, while the gas is relatively metal-poor, suggesting that the central gas may have been diluted by an inflow of lower-metallicity material. One possible explanation is the inflow of metal-poor gas to the centres of concentrated systems, which could dilute the central gas-phase abundance while the stellar component that sets $\Sigma_\star$ remains metal-rich. This is broadly consistent with Cano-Díaz et al. (2025), who find that stellar population gradients in MaNDala galaxies reflect the degree of inside-out versus outside-in formation, with more concentrated systems showing more centrally concentrated star formation histories. We caution, however, that the modest effect size means that this interpretation should be treated as tentative pending confirmation with higher-resolution data. We show in Appendix A that the concentration correlation is not a spatial resolution artefact, with the partial correlation at fixed $R_e/\theta_{\mathrm{PSF}}$ actually strengthening to $r = 0.359$.

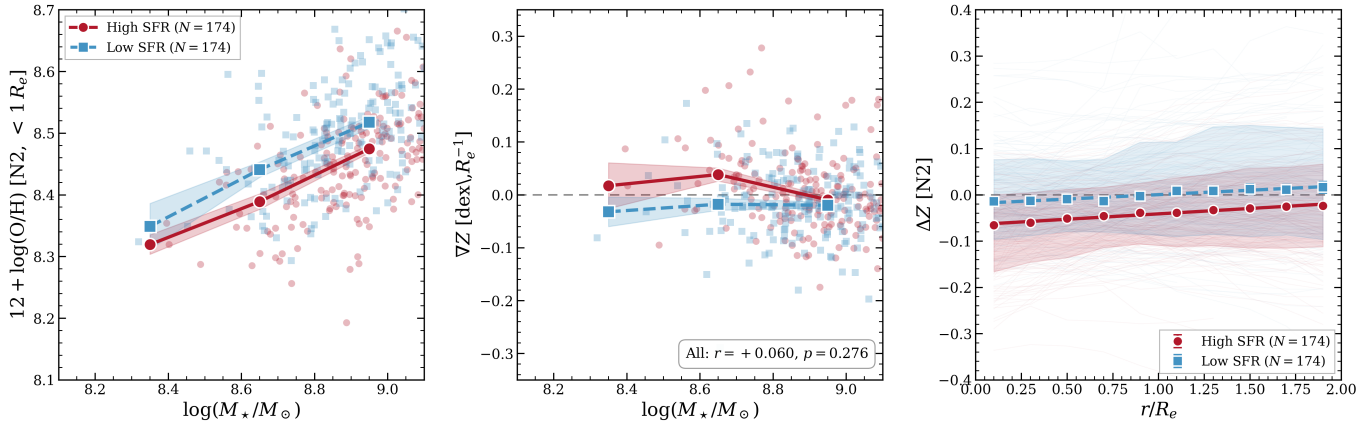


Fig. 7. As Figure 5, but split at the median star formation rate, log(SFR) = −0.952, into high-SFR (red circles, solid) and low-SFR (blue squares, dashed) mass-matched subsamples. The left panel recovers the MZR with no clear dependence on SFR. The centre panel shows a weak and not significant correlation between SFR and the raw gradient slope on the mass-matched subsamples ($r = +0.060$, $p = 0.276$). The right panel shows that the high-SFR group has a more metal-poor centre and a more positive residual gradient than the low-SFR group. The trend is in the same sense as for concentration, but the per-galaxy correlation is weak.

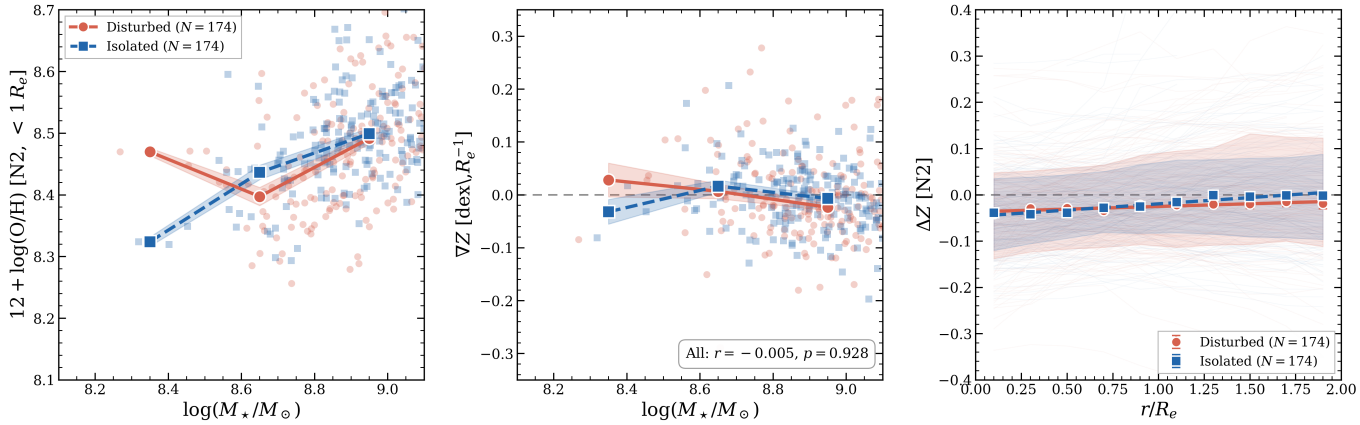


Fig. 8. As Figure 5, but split by visual environmental classification into disturbed (red circles, solid) and isolated (blue squares, dashed) mass-matched subsamples. No significant difference appears in any panel: the left panel shows the same overall metallicity level for both groups, the centre panel shows no correlation between classification and the raw gradient slope ($r = -0.005$, $p = 0.928$), and the right panel shows residual profiles that overlap at all radii. This is a robust null result across all environment indicators tested, indicating that the large-scale environment does not measurably influence the radial distribution of metals.

5.3. A connection with gas velocity dispersion

The gas velocity dispersion within $1\,R_e$, $\sigma_{\rm gas}$ (Figure 6), shows a statistically significant association with the residual gradient when the sample is split at the median of $72.5\,{\rm km\,s^{-1}}$. The left panel shows that the high- and low-$\sigma_{\rm gas}$ groups follow the same MZR, so the overall metallicity level does not vary with $\sigma_{\rm gas}$. The middle panel shows that the high-dispersion group tends to have more positive raw gradient slopes ($r = 0.184$, $p = 0.001$), with little variation with stellar mass. The right panel shows the same trend in the residual (Pearson $r = 0.204$, Spearman $r = 0.289$, $r^2 = 0.041$, $p < 0.001$). The high-dispersion group has inner $\Delta Z = -0.048$ rising to $+0.014$ on the outskirts, with median $\nabla\Delta Z = +0.045$ against $+0.004\,{\rm dex}\,R_e^{-1}$ for the low-dispersion group.

We note that $\sigma_{\rm gas}$ as measured from the MaNGA data shows some dependence on spatial resolution, and beam smearing may contribute to the measured dispersion in poorly resolved galaxies. This limits our ability to draw strong physical conclusions from this correlation, and the result should be regarded as suggestive rather than definitive pending higher-resolution observations.

If the correlation is physical, one possible interpretation is that high $\sigma_{\rm gas}$ traces turbulence driven by strong stellar feedback, which drives outflows that transport metals from the centre towards the outskirts, raising the outer metallicity relative to the centre and producing the more positive residual gradient. Concentration and $\sigma_{\rm gas}$ are uncorrelated ($r = 0.028$, $p = 0.677$), so if both effects are physical they act as independent channels rather than a single underlying driver.

5.4. The absence of environmental effects

We find no significant association between the large-scale environment and the residual gradient slope (Figure 8). The number of neighbours, the group size, the group membership, and the visual classification into isolated and disturbed galaxies all fail to produce a significant correlation in either the Pearson or Spearman tests (Figure 9). Our groups are well populated on both sides (189 disturbed and 177 isolated in the clean sample), so this is

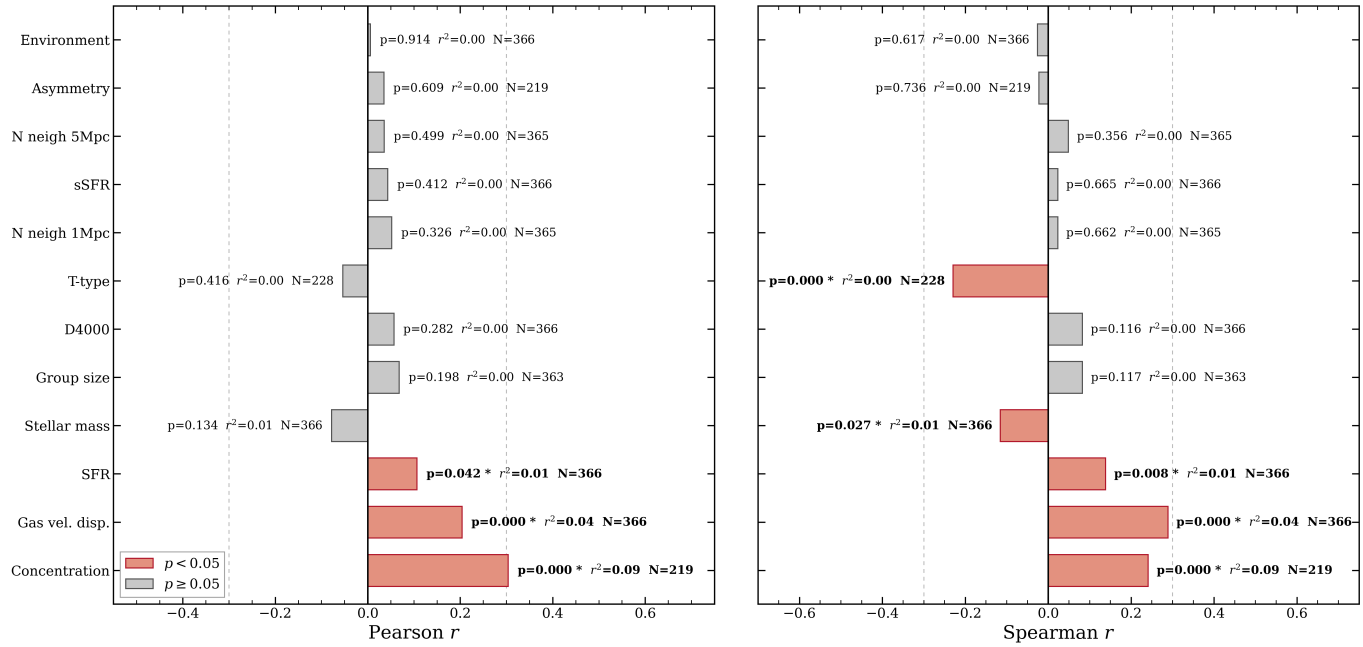


Fig. 9. Summary of the Pearson (left) and Spearman (right) correlation coefficients between the residual gradient slope, $\nabla\Delta Z$ (Section 3.9), and all the physical properties we test, over the clean sample of 366 galaxies, sorted by absolute Pearson r. Coloured bars are significant at $p < 0.05$ and grey bars are not. The p value, coefficient of determination, r^2, and sample size, N, are annotated for each property. Light concentration shows the strongest and most significant association in both tests. The gas velocity dispersion shows a significant correlation that should be interpreted with caution given its sensitivity to spatial resolution (Section 5.3). Morphological T-type shows a significant Spearman correlation but not a significant Pearson correlation, suggesting a weak non-linear association connected to the concentration result (Section 5.6). The large-scale environment and the remaining properties show no significant effect in either test. These are the headline correlations with the residual slope, distinct from the raw-slope correlations annotated in the middle panels of the three-panel figures.

a robustly constrained null rather than a limitation of sample size. We note that this result may depend on how environment is defined. A quantitative classification based on the CAS parameters, for example, may not give the same result as our visual morphology classification.

Across the mass range we probe, these galaxies are predominantly low-density field systems. For such galaxies the internal baryonic physics, which includes the spatial concentration of star formation and the turbulent state of the gas, may dominate over external processes in shaping the radial distribution of metals. Ram-pressure stripping and tidal interactions (Boselli et al. 2022) may become important at higher densities or in cluster environments, but our sample contains too few cluster members to test this regime directly.

5.5. The star formation rate connection

The total star formation rate, split at the sample median (Figure 7), shows only a marginal association with the residual gradient slope. The left panel shows that the high- and low-SFR groups follow the same mass-metallicity relation, so the overall metallicity level does not vary with SFR. The middle panel shows that the high-SFR group has slightly more positive raw gradient slopes than the low-SFR group ($r = 0.060$, $p = 0.276$). The right panel shows the residual profiles. The high-SFR group has a more metal-poor centre, with inner $\Delta Z = -0.062$ rising to -0.024 on the outskirts, and a median residual slope of $\nabla\Delta Z = +0.036$ dex R_e^{-1}. The low-SFR group has a less depressed centre (inner $\Delta Z = -0.018$) and a shallower median slope of $+0.010$ dex R_e^{-1}. This is qualitatively similar to the trend seen for gas velocity dispersion, and could be consistent with a picture in which higher SFR drives stronger feedback and outflows that transport metals outwards.

We treat this result with caution. The per-galaxy correlation is weak (Pearson $r = 0.106$, $p = 0.042$; Spearman $r = 0.138$, $p = 0.008$; $r^2 = 0.011$), with SFR accounting for only 1 percent of the variance in $\nabla\Delta Z$. The trend is also difficult to disentangle from stellar mass, since SFR and stellar mass are correlated through the star-forming main sequence and a weak residual mass effect could appear as a weak SFR correlation. We therefore do not claim an independent physical effect of the star formation rate on metallicity gradients, and regard the correlation as suggestive at most.

5.6. Other parameters

Figure 9 shows the Pearson and Spearman correlation coefficients and r^2 effect sizes for every property we tested, with the significant ones marked in colour. Concentration shows the strongest and most significant association, the star formation rate sits at the margin of significance, and the gas velocity dispersion shows a significant correlation that should be interpreted with caution given its sensitivity to spatial resolution (Section 5.3). All other parameters show no significant effect in both Pearson and Spearman tests, with one exception noted below.

The environmental measures from the GEMA catalogue, which are the group size, the number of neighbours, and the group membership (Section 2.3), are all consistent with no correlation. This agrees with the absence of environmental effects in Section 5.4. The internal properties, which are the specific star formation rate, the D4000 break strength, together with

asymmetry (Section 3.10), are also uncorrelated with the residual gradient in both tests.

The morphological T-type shows no significant Pearson correlation ($r = -0.054$, $p = 0.416$) but a significant Spearman correlation ($r_S = -0.230$, $p < 0.001$, $N = 228$), indicating a weak rank correlation between earlier morphological type and more positive residual gradients. This result is likely connected to the concentration result, since concentration and T-type are physically linked, more concentrated galaxies tend to have earlier morphological types. We therefore do not treat this as an independent result but note it as consistent with the concentration finding. Taken together, these results suggest that the radial distribution of metals in low-mass galaxies is more closely linked to internal structural properties than to the morphology, star formation history, or large-scale environment, though the modest effect sizes indicate that no single parameter is a dominant driver.

5.7. Comparison with previous work

Our results broadly agree with the stellar population gradient results of Cano-Díaz et al. (2025) for the overlapping MaNDala sample. They find mildly negative luminosity-weighted gradients and flat to slightly positive mass-weighted stellar metallicity gradients, which are qualitatively consistent with our flat gas-phase gradients.

The average gradient is flat, but when we split the sample by properties that may trace internal gas flows and stellar feedback, namely concentration, gas velocity dispersion, and star formation rate, tentative trends appear. Galaxies with a higher concentration, higher gas velocity dispersion, and higher star formation rate tend to show more positive residual gradients, though the effect sizes are modest ($r^2 \leq 0.092$) and no single parameter accounts for more than 9 percent of the variance in $\nabla\Delta Z$. We note that the gas velocity dispersion result should be treated with caution given its sensitivity to spatial resolution (Section 5.3). One possible interpretation is a picture in which feedback-driven outflows and inflows continually redistribute metals in these shallow potential wells (Mercado et al. 2021), with galaxies caught at different phases of this cycle showing different gradient slopes. The flat average would then be the long-term outcome, while the property trends pick out galaxies in the act of redistributing their metals. We caution, however, that the modest effect sizes and the sensitivity of some results to the PSF resolution cut mean that this interpretation remains speculative, and confirmation with larger samples and higher-resolution data would be valuable. Our results are also broadly consistent with recent dedicated IFU studies of dwarf galaxies (Li et al. 2025; Valé et al. 2025), which find similarly flat or mildly negative gradients in this mass regime.

6. Conclusions

We have presented spatially resolved gas-phase metallicity gradients for 382 star-forming low-mass galaxies selected from the complete MaNGA DR17 survey (Abdurro'uf et al. 2022). This is the largest spatially resolved spectroscopic study of dwarf galaxy metallicity gradients to date. Our main conclusions are as follows.

1. Metallicity gradients are flat on average, with a median slope of $-0.007\,\mathrm{dex}\,R_\mathrm{e}^{-1}$ and a galaxy-to-galaxy scatter of $0.071\,\mathrm{dex}\,R_\mathrm{e}^{-1}$. The slopes are distributed broadly about zero, consistent with a balance of mild positive and negative gradients rather than uniformly flat profiles. Beam smearing in the less well-resolved galaxies may contribute to this flattening; a stricter resolution cut ($R_\mathrm{e} \geq 2\,\theta_\mathrm{PSF}$, $N = 254$) yields a more negative median slope of $-0.026\,\mathrm{dex}\,R_\mathrm{e}^{-1}$ (Appendix A).
2. The N2 calibration of Pettini & Pagel (2004) recovers a significant MZR for our sample (Pearson $r = 0.444$, $r^2 = 0.197$, $N = 380$). For the subset of 379 galaxies with a valid O3N2 measurement, one galaxy (8934−9102) is excluded because its N2-derived metallicity is unphysically high ($12 + \log(\mathrm{O/H}) = 9.20$), likely reflecting a failed fit rather than a true abundance. On this subsample the N2 correlation strengthens to $r = 0.473$, while O3N2 gives $r = 0.380$, confirming N2 as the more reliable indicator for this low-mass regime (Appendix F).
3. We find a significant positive correlation between the gas-phase metallicity and the local stellar mass surface density, $\Sigma_\star$ (Pearson $r = 0.371$, $r^2 = 0.138$), indicating that denser regions tend to be more metal-rich, though local surface density accounts for only 14 percent of the observed variance. The linearity of this relation and a small systematic correction applied to the residual profiles are discussed in Appendix B.
4. After removing the $\Sigma_\star$ dependence, the residual metallicity, ΔZ, retains a clear mass offset at all radii. More massive galaxies tend to be more metal-rich than their local density predicts, and less massive galaxies more metal-poor. Total stellar mass therefore sets the overall enrichment level, but shows no significant Pearson correlation with the residual gradient slope ($r_P = -0.078$, $r^2 = 0.006$, $p = 0.134$), though the Spearman test gives a marginally significant result ($r_S = -0.116$, $p = 0.027$).
5. The strongest association with the residual gradient slope, $\nabla\Delta Z$, is light concentration, C (Pearson $r = 0.304$, Spearman $r = 0.241$, $r^2 = 0.092$, $p < 0.001$), though concentration accounts for only 9 percent of the variance. More concentrated galaxies tend to have more positive residual gradients, with centres that are metal-poor relative to what their high local stellar density predicts. Monte Carlo error propagation confirms the result is robust to measurement uncertainties (68 percent CI: $r \in [0.283, 0.313]$; Appendix E). The result persists with a stricter PSF resolution cut, though with a reduced effect size ($r = 0.234$, $p = 0.006$; Appendix A).
6. Gas velocity dispersion, σ_gas, shows a statistically significant positive correlation (Pearson $r = 0.204$, Spearman $r = 0.289$, $r^2 = 0.041$, $p < 0.001$), and the star formation rate shows a weaker association (Pearson $r = 0.106$, Spearman $r = 0.138$, $r^2 = 0.011$, $p = 0.042$). We caution that the σ_gas result shows some sensitivity to spatial resolution and should be interpreted cautiously pending higher-resolution observations (Section 5.3).
7. The large-scale environment has no significant effect on the residual gradient slope. The visual classification into disturbed and isolated galaxies (189 and 177 galaxies respectively), and all quantitative environment indicators from the GEMA catalogue, show no significant correlation in either Pearson or Spearman tests, which is a robust null result.

Taken together, these results suggest that internal structural properties, particularly light concentration, are more closely linked to the radial distribution of metals in low-mass galaxies than the stellar mass, star formation history, or large-scale environment. The modest effect sizes ($r^2 \leq 0.092$) indicate that no single parameter is a dominant driver and that much of the galaxy-to-galaxy scatter remains unexplained. The flat average gradient combined with the tentative trends in the concentration, gas

velocity dispersion, and star formation rate is broadly consistent with a picture in which feedback-driven processes redistribute metals in shallow potential wells (Mercado et al. 2021), though confirmation with larger samples and a higher spatial resolution would be needed to establish this interpretation on firmer ground. The large-scale environment plays no detectable role across the mass range we probe, suggesting that these galaxies are shaped primarily by their own internal evolution rather than by their surroundings.

Data availability

The full version of Table G.1 is available at the CDS via https://cdsarc.cds.unistra.fr/viz-bin/cat/J/A+A/715/A225

Acknowledgements. We thank the anonymous referee for a thorough and constructive report that significantly improved the quality and rigour of this work. A.D. acknowledges support from ANID through the Beca de Doctorado Nacional, Folio 21260921. S.S. and R.C. thank ANRF for financial support through the SERB-SURE grants (SUR/2022/001789 and SUR/2022/001503, respectively), and IUCAA for their hospitality and usage of their facilities during their stay at different times as part of the university associateship programme. R.C. thanks ANRF for an ARG grant (ANRF/ARG/2025/003315/PS). This work uses data from the Sloan Digital Sky Survey IV, funded by the Alfred P. Sloan Foundation, the U.S. Department of Energy Office of Science, and the Participating Institutions (https://www.sdss4.org). It also uses data from the DESI Legacy Imaging Surveys (DECaLS, BASS, and MzLS) and NEOWISE. This research made use of ASTROPY (Astropy Collaboration 2013), NUMPY (Harris et al. 2020), SCIPY (Virtanen et al. 2020), and MATPLOTLIB (Hunter 2007).

References

Abdurro'uf, Accetta, K., Aerts, C., et al. 2022, ApJS, 259, 35
Abraham, R. G., van den Bergh, S., Glazebrook, K., et al. 1996, ApJS, 107, 1
Acharyya, A., Krumholz, M. R., Federrath, C., et al. 2020, MNRAS, 495, 3819
Andrews, B. H., & Martini, P. 2013, ApJ, 765, 140
Argudo-Fernández, M., Verley, S., Bergond, G., et al. 2015, A&A, 578, A110
Astropy Collaboration (Robitaille, T. P., et al.) 2013, A&A, 558, A33
Barrera-Ballesteros, J. K., Heckman, T. M., Zhu, G. B., et al. 2016, MNRAS, 463, 2513
Belfiore, F., Maiolino, R., Tremonti, C., et al. 2017, MNRAS, 469, 151
Blanton, M. R., Schlegel, D. J., Strauss, M. A., et al. 2005, AJ, 129, 2562
Blanton, M. R., Kazin, E., Muna, D., Weaver, B. A., & Price-Whelan, A. 2011, AJ, 142, 31
Blanton, M. R., Bershady, M. A., Abolfathi, B., et al. 2017, AJ, 154, 28
Boissier, S., & Prantzos, N. 1999, MNRAS, 307, 857
Boselli, A., Fossati, M., & Sun, M. 2022, A&ARv, 30, 3
Bundy, K., Bershady, M. A., Law, D. R., et al. 2015, ApJ, 798, 7
Cano-Díaz, M., Hernández-Toledo, H. M., Rodríguez-Puebla, A., et al. 2022, AJ, 164, 127
Cano-Díaz, M., Rodríguez-Puebla, A., Robleto-Orús, A. C., et al. 2025, AJ, 170, 27
Cappellari, M. 2017, MNRAS, 466, 798
Chabrier, G. 2003, PASP, 115, 763
Conselice, C. J. 2003, ApJS, 147, 1
Drory, N., MacDonald, N., Bershady, M. A., et al. 2015, AJ, 149, 77
Elbaz, D., Daddi, E., Le Borgne, D., et al. 2007, A&A, 468, 33
Grossi, M., García-Benito, R., Cortesi, A., et al. 2020, MNRAS, 498, 1939
Gunn, J. E., Siegmund, W. A., Mannery, E. J., et al. 2006, AJ, 131, 2332
Harris, C. R., Millman, K. J., van der Walt, S. J., et al. 2020, Nature, 585, 357
Hunter, J. D. 2007, Comput. Sci. Eng., 9, 90
Kennicutt, R. C. 1998, ARA&A, 36, 189
Kewley, L. J., & Ellison, S. L. 2008, ApJ, 681, 1183
Kewley, L. J., Rupke, D., Zahid, H. J., Geller, M. J., & Barton, E. J. 2010, ApJ, 721, L48
Law, D. R., Yan, R., Bershady, M. A., et al. 2015, AJ, 150, 19
Law, D. R., Cherinka, B., Yan, R., et al. 2016, AJ, 152, 83
Li, T., Zhang, H.-X., Lyu, W., et al. 2025, A&A, 698, A208
Lupton, R., Blanton, M. R., Fekete, G., et al. 2004, PASP, 116, 133
Maiolino, R., & Mannucci, F. 2019, A&ARv, 27, 3
Mannucci, F., Cresci, G., Maiolino, R., Marconi, A., & Gnerucci, A. 2010, MNRAS, 408, 2115
Matteucci, F., & Francois, P. 1989, MNRAS, 239, 885
Mercado, F. J., Bullock, J. S., Boylan-Kolchin, M., et al. 2021, MNRAS, 501, 5121
Moustakas, J., Kennicutt, R. C., Tremonti, C. A., et al. 2010, ApJS, 190, 233
Pettini, M., & Pagel, B. E. J. 2004, MNRAS, 348, L59
Poetrodjojo, H., Groves, B., Kewley, L. J., et al. 2021, MNRAS, 502, 3357
Rosales-Ortega, F. F., Sánchez, S. F., Iglesias-Páramo, J., et al. 2012, ApJ, 756, L31
Rupke, D. S. N., Kewley, L. J., & Barnes, J. E. 2010, ApJ, 710, L156
Samui, S., Subramanian, K., & Srianand, R. 2008, MNRAS, 385, 783
Sánchez, S. F. 2020, ARA&A, 58, 99
Sánchez, S. F., Rosales-Ortega, F. F., Jungwiert, B., et al. 2013, A&A, 554, A58
Sánchez, S. F., Rosales-Ortega, F. F., Iglesias-Páramo, J., et al. 2014, A&A, 563, A49
Sánchez, S. F., Pérez, E., Sánchez-Blázquez, P., et al. 2016, Rev. Mexicana Astron. Astrofis., 52, 21
Sánchez-Blázquez, P., Peletier, R. F., Jiménez-Vicente, J., et al. 2006, MNRAS, 371, 703
Smee, S. A., Gunn, J. E., Uomoto, A., et al. 2013, AJ, 146, 32
Storey, P. J., & Zeippen, C. J. 2000, MNRAS, 312, 813
Tolstoy, E., Hill, V., & Tosi, M. 2009, ARA&A, 47, 371
Tremonti, C. A., Heckman, T. M., Kauffmann, G., et al. 2004, ApJ, 613, 898
Valé, G., Lara-López, M. A., Valerdi, M., et al. 2025, A&A, 701, A226
Vázquez-Mata, J. A., Hernández-Toledo, H. M., Avila-Reese, V., et al. 2022, MNRAS, 512, 2222
Veilleux, S., Cecil, G., & Bland-Hawthorn, J. 2005, ARA&A, 43, 769
Virtanen, P., Gommers, R., Oliphant, T. E., et al. 2020, Nat. Meth., 17, 261
Westfall, K. B., Cappellari, M., Bershady, M. A., et al. 2019, AJ, 158, 231
Wisz, M. E., Masters, K. L., Daniel, K. J., Stark, D. V., & Belfiore, F. 2025, ApJ, 983, 57
Zaritsky, D., Kennicutt, R. C., & Huchra, J. P. 1994, ApJ, 420, 87

Appendix A: PSF smearing analysis

To verify that our gradient measurements are not significantly affected by beam smearing from the MaNGA point spread function (PSF, $\theta_{\rm PSF} = 2.5$ arcsec FWHM), we carried out six tests.

Unresolved versus resolved galaxies. We compared the distribution of gradient slopes for spatially unresolved galaxies ($R_{\rm e} < 1 \times \theta_{\rm PSF}$, $N = 8$) with that of the resolved galaxies ($R_{\rm e} \geq 1 \times \theta_{\rm PSF}$, $N = 382$). Unresolved galaxies show a systematic bias towards positive gradient slopes (median $+0.034\,{\rm dex}\,R_{\rm e}^{-1}$) relative to resolved galaxies (median $-0.007\,{\rm dex}\,R_{\rm e}^{-1}$; Mann–Whitney $p = 0.015$), confirming that the $R_{\rm e} \geq 1 \times \theta_{\rm PSF}$ cut is necessary. This is the expected signature of beam smearing, where light from the metal-rich central regions is spread into outer bins by the PSF, artificially producing a spuriously positive gradient (Acharyya et al. 2020).

Residual dependence on resolution. Panel (c) of Figure A.1 shows the residual metallicity gradient slope $\nabla\Delta Z$ as a function of $R_{\rm e}/\theta_{\rm PSF}$ for the full resolved sample. Even within the resolved sample we find a significant negative correlation ($r = -0.450$, $p < 0.001$), meaning that galaxies closer to the PSF limit still have systematically more positive residual gradients. This residual dependence motivates a stricter resolution cut. The trend flattens noticeably above $R_{\rm e} \geq 2 \times \theta_{\rm PSF}$, which we adopt as a robustness threshold.

Stability of results with stricter resolution cuts. Table A.1 shows how our key results change as we apply progressively stricter resolution cuts. The concentration correlation remains significant at $R_{\rm e} \geq 2 \times \theta_{\rm PSF}$ ($r = 0.234$, $r^2 = 0.055$, $p = 0.006$, $N = 254$) and the median gradient slope stabilises around -0.026 to $-0.034\,{\rm dex}\,R_{\rm e}^{-1}$, more negative than the full-sample value of $-0.007\,{\rm dex}\,R_{\rm e}^{-1}$ because beam smearing was artificially flattening the gradients in the less well resolved galaxies. We therefore adopt the full 382 galaxy sample as our primary sample throughout the paper, and note that the main scientific conclusions are robust to applying the stricter $R_{\rm e} \geq 2 \times \theta_{\rm PSF}$ cut.

Fitting gradients over PSF-unaffected radial ranges. For each galaxy we identified the bins whose centres lie within one PSF FWHM of the galaxy centre and refitted the gradients using only the outer bins, excluding on average 2.2 bins per galaxy. If beam smearing were confined to the innermost bins, this test would eliminate the bias. The correlation between $\nabla\Delta Z$ and $R_{\rm e}/\theta_{\rm PSF}$ actually strengthens slightly with this approach ($r = -0.479$ versus $r = -0.450$ for the full radial range), indicating that the PSF effect is not confined to the innermost bins but reflects a more general smearing of the gradient measurement in poorly resolved galaxies. This reinforces the need for the stricter resolution cut rather than resolving the issue through bin exclusion alone.

Inclination. We find no significant correlation between galaxy inclination and either ∇Z ($r = -0.036$, $p = 0.49$) or $\nabla\Delta Z$ ($r = -0.009$, $p = 0.86$), confirming that inclination effects do not bias our gradient measurements.

Partial correlation of concentration at fixed resolution. A potential concern is that the concentration correlation with $\nabla\Delta Z$ could be driven by a hidden dependence on spatial resolution, if more concentrated galaxies happened to be better resolved. We tested this by first checking whether concentration C correlates with $R_{\rm e}/\theta_{\rm PSF}$ in our sample. We find no significant correlation ($r = 0.038$, $p = 0.572$, $N = 219$), confirming that concentrated galaxies are not preferentially better or worse resolved than less concentrated ones. We then computed the partial correlation between C and $\nabla\Delta Z$ after removing the linear dependence of both quantities on $R_{\rm e}/\theta_{\rm PSF}$. The partial correlation is $r = 0.359$ ($r^2 = 0.129$, $p < 0.001$), stronger than the raw correlation of $r = 0.304$, demonstrating that the concentration correlation is not a resolution artefact.

This finding may appear to be in tension with the monotonic decline of the concentration correlation in Table A.1 ($r = 0.304 \rightarrow 0.294 \rightarrow 0.234 \rightarrow 0.141 \rightarrow 0.123$ as the resolution cut tightens). However the two tests measure different things. The partial correlation removes the smooth linear trend of $\nabla\Delta Z$ with $R_{\rm e}/\theta_{\rm PSF}$ while retaining the full sample of $N = 219$ galaxies with concentration measurements. The stability table instead restricts to progressively smaller and better-resolved subsamples, reducing N from 219 to 181 to 137 to 103 to 66. The weakening in Table A.1 is therefore consistent with reduced statistical power at smaller sample sizes rather than a physical resolution dependence, and the partial correlation provides the more direct test of whether spatial resolution drives the result. The results are shown in Figure A.1.

Appendix B: Linearity of the Z–$\Sigma_\star$ relation

The residual metallicity ΔZ is defined by subtracting the prediction of a global linear fit to the $Z - \log\Sigma_\star$ relation (Section 3.8). The results of the linearity test are shown in Figure B.1.

First, we compared the root-mean-square residuals (RMSE) of three fits to the $Z - \log\Sigma_\star$ relation across all 3608 valid bins: a linear fit (RMSE = 0.1014 dex), a quadratic fit (RMSE = 0.1011 dex, improvement 0.3 percent), and a piecewise linear fit with a break at the median $\log\Sigma_\star$ (RMSE = 0.1008 dex, improvement 0.6 percent). The non-linear fits are negligibly better than the linear fit, and we therefore retain the simpler linear parametrisation.

Second, we tested whether the residuals of the linear fit show a systematic trend with radius. We find a weak but significant positive trend of $+0.017\,{\rm dex}\,R_e^{-1}$ in the median residuals across the ten radial bins ($r = 0.939$, $p < 0.001$). This artificial trend arises because the linear fit slightly overestimates metallicity in the inner high-$\Sigma_\star$ bins and underestimates it in the outer low-$\Sigma_\star$ bins. We correct for this by subtracting $+0.017 \times (r/R_e)$ from each ΔZ value before fitting the residual gradient slopes. After this correction the median ΔZ slope changes from $+0.044$ to $+0.001\,{\rm dex}\,R_e^{-1}$, consistent with zero, and the concentration correlation is completely unchanged ($r = 0.304$, $p < 0.001$ before and after correction). All ΔZ slopes reported in the main text use this corrected definition.

Appendix C: Metallicity and stellar mass surface density

Figure C.1 shows the relationship between gas-phase metallicity and local stellar mass surface density $\Sigma_\star$ for all 3608 valid radial bins from all 382 galaxies. The significant positive correlation ($r = 0.371$, $p = 2.0 \times 10^{-118}$) confirms that denser regions are on average more metal rich, consistent with more chemically evolved stellar populations at higher surface densities. The two mass groups are systematically offset in metallicity at fixed $\Sigma_\star$, motivating the residual metallicity analysis

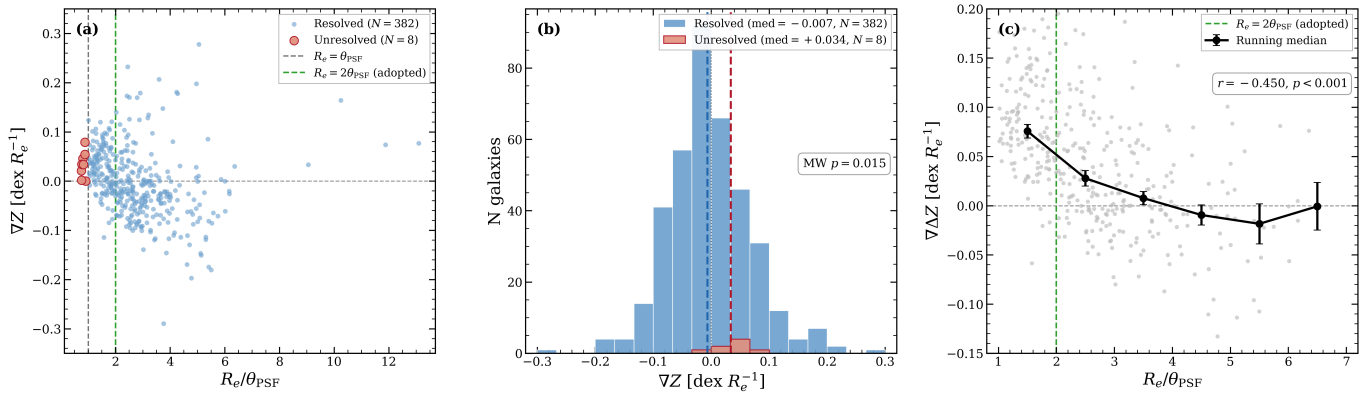


Fig. A.1. PSF beam smearing analysis. Panel (a): metallicity gradient slope ∇Z as a function of R_e/θ_{PSF} for resolved (blue, $N = 382$) and unresolved (red, $N = 8$) galaxies. The dashed vertical lines mark $R_e = 1\,\theta_{PSF}$ (grey) and $R_e = 2\,\theta_{PSF}$ (green, adopted robustness cut). Panel (b): histogram of ∇Z for unresolved (red) and resolved (blue) galaxies. Unresolved galaxies are biased towards positive slopes (median +0.034 dex R_e^{-1}) relative to resolved galaxies (median −0.007 dex R_e^{-1}; Mann–Whitney $p = 0.015$). Panel (c): residual gradient slope $\nabla\Delta Z$ as a function of R_e/θ_{PSF} for the full resolved sample. The black line shows the running median. Even within the resolved sample the gradient correlates with resolution ($r = -0.450$, $p < 0.001$), motivating the stricter $R_e \geq 2\,\theta_{PSF}$ cut shown by the green dashed line.

Table A.1. Stability of key results with progressively stricter PSF resolution cuts.

Cut	N	$\langle\nabla Z\rangle$ (dex R_e^{-1})	r_C	r_C^2	p_C	r_{SFR}	p_{SFR}	p_{env}
$\geq 1.0\,\theta_{PSF}$	382	−0.007	0.304	0.092	< 0.001	0.106	0.042	0.616
$\geq 1.5\,\theta_{PSF}$	323	−0.020	0.294	0.087	< 0.001	0.123	0.031	0.985
$\geq 2.0\,\theta_{PSF}$	254	−0.026	0.234	0.055	0.006	0.149	0.021	0.331
$\geq 2.5\,\theta_{PSF}$	194	−0.034	0.141	0.020	0.154	0.153	0.040	0.612
$\geq 3.0\,\theta_{PSF}$	131	−0.031	0.123	0.015	0.326	0.058	0.529	0.473

Notes. Columns give the resolution threshold, total number of galaxies, median metallicity gradient slope, and Pearson correlation coefficients with their effect sizes (r^2) and p values for light concentration C and star formation rate, and the Mann–Whitney p value for the visual environment classification.

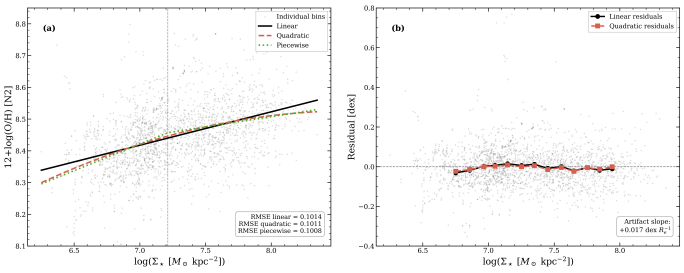


Fig. B.1. Test of the linearity of the $Z-\log\Sigma_\star$ relation. Left: comparison of linear (black), quadratic (red dashed), and piecewise linear (green dotted) fits to the 3608 valid bins. The three fits are visually indistinguishable. Right: running median of the residuals from the linear (black) and quadratic (red) fits as a function of $\log\Sigma_\star$. The linear fit shows a small systematic trend of +0.017 dex R_e^{-1} which we correct for as described in the text.

described in Section 3.8. The linearity of this relation and the small systematic correction applied to the residuals are discussed in Appendix B. To quantify whether the two mass groups are genuinely offset in ΔZ at fixed $\Sigma_\star$, we compared the ΔZ distributions for all valid bins in the high-mass ($\log(M_\star/M_\odot) \geq 8.89$, 1827 bins) and low-mass ($\log(M_\star/M_\odot) < 8.89$, 1781 bins) groups. The high-mass group has a median $\Delta Z = -0.004$ and the low-mass group a median of −0.051, an offset of +0.047 dex. A Mann-Whitney test confirms the offset is highly significant ($p < 0.001$), demonstrating that total stellar mass influences chemical enrichment independently of local stellar mass surface density.

Appendix D: Diffuse ionised gas test

Diffuse ionised gas (DIG) can bias emission-line metallicity measurements because its line ratios differ from those of star-forming H II regions. To assess whether DIG contamination introduces a systematic bias into our gradient measurements, we performed a half-ellipse test. For each galaxy we split the IFU spaxels into two halves along the minor axis and measured the metallicity gradient slope independently on each half. In the absence of systematic DIG contamination, the two halves should give consistent gradients with differences distributed symmetrically around zero.

We applied this test to all 382 galaxies, obtaining valid gradient measurements for both halves in 358 galaxies. The two halves show a strong positive correlation ($r = 0.631$, $p < 0.001$), confirming that the gradient measurements are physically consistent across both sides of each galaxy. The differences between the two halves have a median of −0.002 dex R_e^{-1}, consistent with zero (one-sample t-test $p = 0.578$), and 91 percent of galaxies show absolute differences smaller than 0.10 dex R_e^{-1}. The results are shown in Figure D.1.

These results confirm that DIG contamination does not introduce a systematic bias into our gradient measurements.

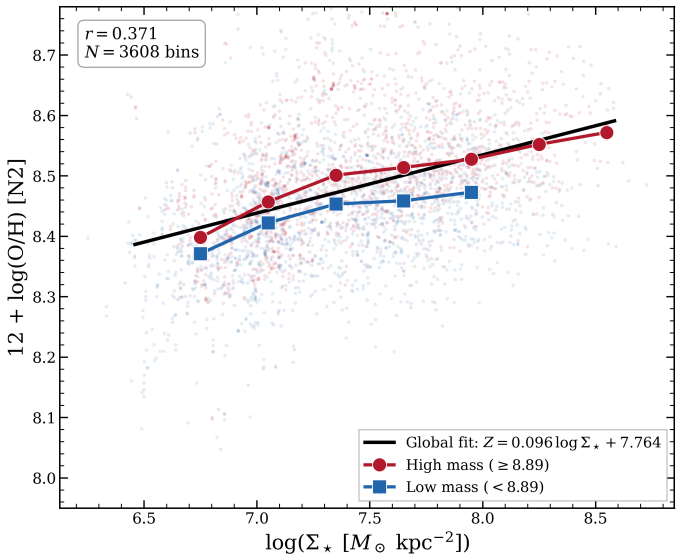


Fig. C.1. Gas-phase metallicity as a function of local stellar mass surface density $\Sigma_\star$ for all 3608 valid radial bins from all 382 galaxies. Points are colour coded by stellar mass group: high mass ($\log(M_\star/M_\odot) \geq 8.89$, red, $N = 191$ galaxies) and low mass ($\log(M_\star/M_\odot) < 8.89$, blue, $N = 191$ galaxies). The solid line shows the global linear fit $Z = 0.0963 \log(\Sigma_\star) + 7.7643$ (Pearson $r = 0.371$, $p = 2.0 \times 10^{-118}$, $N = 3608$ bins), used to define the residual metallicity ΔZ in Section 3.8. The filled circles and squares show the running median for the high and low mass groups respectively. The two mass groups are offset in metallicity at all values of $\log(\Sigma_\star)$, demonstrating that total stellar mass influences chemical enrichment independently of local stellar mass surface density.

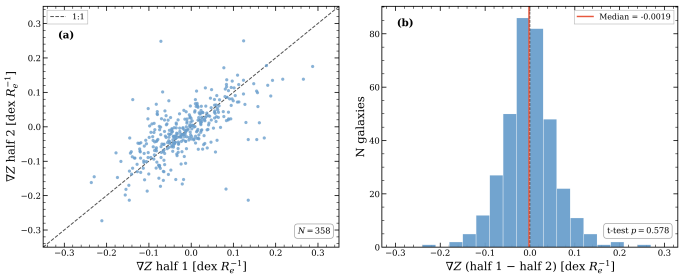


Fig. D.1. Half-ellipse test for diffuse ionised gas contamination. For each galaxy the IFU is split into two halves along the minor axis and the metallicity gradient slope is measured independently on each half. Panel (a): gradient slope measured on half 1 versus half 2 for 358 galaxies. The dashed line shows the 1:1 relation. The strong correlation ($r = 0.631$, $p < 0.001$) confirms physically consistent measurements across both halves. Panel (b): histogram of the difference between the two half slopes. The distribution is symmetric around zero (median = -0.002 dex R_e^{-1}, t-test $p = 0.578$), confirming the absence of a systematic bias from DIG contamination.

Appendix E: Monte Carlo error propagation

Our primary correlation result is between light concentration C and residual gradient slope $\nabla\Delta Z$. To quantify how sensitive this result is to measurement uncertainties in the gradient slopes, we performed a Monte Carlo analysis on both the full sample and the stricter resolution subsample.

For the full sample of 366 clean galaxies, 219 have both a valid concentration measurement and a well-constrained gradient slope. Of the 230 galaxies with a concentration measurement, 11 fail the gradient quality cut $\sigma_{\nabla\Delta Z} \leq 0.05$ dex R_e^{-1}, leaving 219.

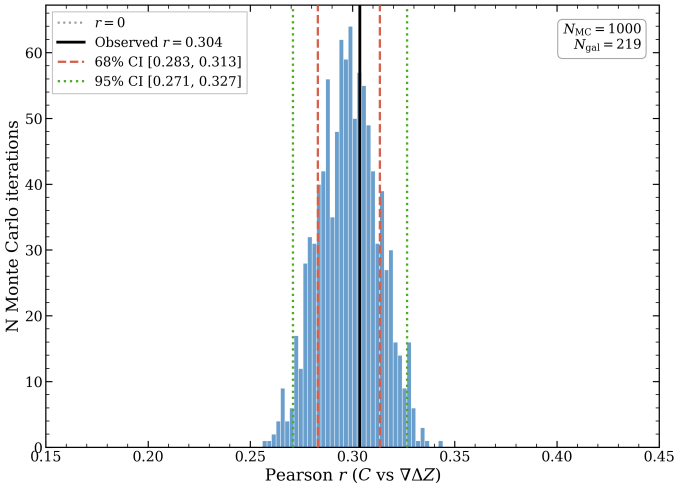


Fig. E.1. Monte Carlo distribution of the Pearson correlation coefficient between light concentration C and residual gradient slope $\nabla\Delta Z$ for the full sample ($N = 219$ galaxies with valid C and $\nabla\Delta Z$ measurements), based on 1000 iterations in which each $\nabla\Delta Z$ value is perturbed within its measurement uncertainty $\sigma_{\nabla\Delta Z}$. The vertical solid black line marks the observed value ($r = 0.304$), the red dashed lines mark the 68 percent confidence interval $[+0.283, +0.313]$, and the green dotted lines mark the 95 percent confidence interval $[+0.271, +0.327]$. The distribution is entirely positive and well separated from zero, confirming the robustness of the concentration correlation.

For each of 1000 iterations we perturbed the $\nabla\Delta Z$ value of each galaxy by a random draw from a Gaussian distribution centred on the measured value with standard deviation equal to $\sigma_{\nabla\Delta Z}$, and recomputed the Pearson correlation coefficient with C. The resulting distribution is shown in Figure E.1.

For the full sample ($N = 219$, $r = 0.304$) the Monte Carlo mean is $r = 0.298$ with a 68 percent confidence interval of $[+0.283, +0.313]$ and a 95 percent confidence interval of $[+0.271, +0.327]$. The entire distribution lies well above zero, confirming the robustness of the concentration correlation to measurement uncertainties.

For the stricter resolution subsample ($R_e \geq 2\,\theta_{PSF}$), 137 of the 254 galaxies have a valid concentration measurement and well-constrained gradient slope ($r = 0.234$); the Monte Carlo mean is $r = 0.239$, equal to the observed value within rounding, with a 68 percent confidence interval of $[+0.214, +0.256]$ and a 95 percent confidence interval of $[+0.191, +0.276]$. Both distributions are entirely positive, confirming that the concentration correlation is robust to measurement uncertainties in both samples.

Appendix F: N2 and O3N2 metallicity calibration comparison

We use the N2 strong-line calibration of Pettini & Pagel (2004) as our primary metallicity indicator throughout this work. To validate this choice we compare the performance of N2 and O3N2 in recovering the MZR for our sample.

Figure F.1 shows the MZR for the 379 galaxies with valid metallicity measurements within $1\,R_e$ in both calibrations. One galaxy (8934-9102) is excluded because its N2-derived metallicity is unphysically high (12 + log(O/H) = 9.20, exceeding the calibration range of Pettini & Pagel 2004), most likely reflecting a failed emission-line fit rather than a true abundance; its O3N2 value is also unphysical (-1.42). The N2 calibration recovers a clear and significant MZR (Pearson $r = 0.473$, $p < 0.001$,

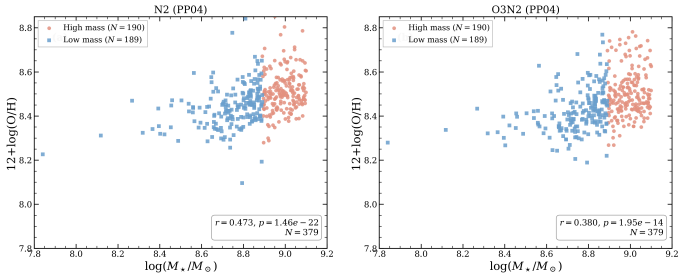


Fig. F.1. Mass-metallicity relation for 379 galaxies in our sample with valid metallicity measurements within 1 R_e, using the N2 (left, Pearson $r = 0.473$, $p < 0.001$) and O3N2 (right, $r = 0.380$, $p < 0.001$) calibrations of Pettini & Pagel (2004). Points are colour coded by stellar mass group: high mass (red circles) and low mass (blue squares). Both calibrations recover a significant MZR, with N2 giving a stronger and cleaner correlation. The N2 calibration is therefore adopted as the primary metallicity indicator throughout this work.

$N = 379$). The O3N2 calibration also recovers a significant MZR but with a weaker correlation ($r = 0.380$, $p < 0.001$, $N = 379$), consistent with the known larger scatter of O3N2 at low metallicities (Kewley & Ellison 2008). The N2 calibration is therefore the more reliable indicator for our low-mass sample and is adopted throughout the main analysis.

Appendix G: Master table

Table G.1. Key properties of the 382 low-mass galaxies in the final sample.

PlateIFU	z	$\log M_\star$ ($M_\odot$)	R_e ($''$)	R_e/θ_{PSF}	$\nabla Z \pm \sigma$ (dex R_e^{-1})	$\nabla \Delta Z \pm \sigma$ (dex R_e^{-1})	Class
11020-12701	0.0002	7.22	32.72	13.09	+0.077 ± 0.018	...	ISOLATED
8150-3701	0.0017	7.57	25.60	10.24	+0.164 ± 0.002	...	DISTURBED
8554-12704	0.0005	7.79	29.68	11.87	+0.074 ± 0.043	...	ISOLATED
9049-6101	0.0139	7.84	7.35	2.94	−0.094 ± 0.023	−0.052 ± 0.027	ISOLATED
8981-12705	0.0057	8.12	6.10	2.44	−0.076 ± 0.013	−0.023 ± 0.016	ISOLATED
8619-12705	0.0116	8.27	7.87	3.15	−0.085 ± 0.016	−0.043 ± 0.013	DISTURBED
9493-12702	0.0122	8.32	7.14	2.86	−0.081 ± 0.008	−0.037 ± 0.009	ISOLATED
8546-12702	0.0125	8.37	6.48	2.59	+0.019 ± 0.012	+0.072 ± 0.014	ISOLATED
9502-6102	0.0173	8.39	7.59	3.03	+0.003 ± 0.016	+0.025 ± 0.022	ISOLATED
8565-6104	0.0094	8.40	4.72	1.89	+0.087 ± 0.012	+0.138 ± 0.012	ISOLATED
9093-1902	0.0220	8.40	3.04	1.22	+0.017 ± 0.012	+0.053 ± 0.015	ISOLATED
8993-6101	0.0196	8.42	7.48	2.99	−0.037 ± 0.008	−0.047 ± 0.008	ISOLATED
8619-12704	0.0206	8.45	5.57	2.23	−0.032 ± 0.008	+0.005 ± 0.013	ISOLATED
8719-9101	0.0178	8.46	12.38	4.95	+0.028 ± 0.050	+0.084 ± 0.047	DISTURBED
8082-3701	0.0213	8.46	2.87	1.15	+0.036 ± 0.007	+0.078 ± 0.008	DISTURBED
8982-12702	0.0250	8.49	6.81	2.72	−0.095 ± 0.011	−0.066 ± 0.006	ISOLATED
8552-3701	0.0183	8.50	4.46	1.78	+0.104 ± 0.015	+0.154 ± 0.018	DISTURBED
9886-6102	0.0219	8.54	6.62	2.65	+0.017 ± 0.016	+0.065 ± 0.017	ISOLATED
8338-1901	0.0215	8.54	3.19	1.28	+0.106 ± 0.017	+0.157 ± 0.019	DISTURBED
8657-6104	0.0175	8.56	5.17	2.07	−0.027 ± 0.010	+0.016 ± 0.009	DISTURBED
8149-6103	0.0221	8.56	5.36	2.14	−0.072 ± 0.015	−0.048 ± 0.010	DISTURBED
11022-12702	0.0228	8.56	6.00	2.40	+0.089 ± 0.017	+0.124 ± 0.014	ISOLATED
9494-6102	0.0157	8.56	6.04	2.41	+0.173 ± 0.033	+0.199 ± 0.038	ISOLATED
8996-6104	0.0214	8.57	6.62	2.65	−0.011 ± 0.008	−0.020 ± 0.008	ISOLATED
9001-12704	0.0212	8.59	8.94	3.58	−0.030 ± 0.015	+0.010 ± 0.020	ISOLATED
8447-1901	0.0202	8.59	3.16	1.27	−0.026 ± 0.005	+0.020 ± 0.004	ISOLATED
8459-9102	0.0170	8.59	7.75	3.10	+0.021 ± 0.016	+0.063 ± 0.017	ISOLATED
8553-12703	0.0136	8.61	12.40	4.96	+0.198 ± 0.053	+0.241 ± 0.056	DISTURBED
9886-3701	0.0216	8.62	12.84	5.13	−0.151 ± 0.091	−0.063 ± 0.098	DISTURBED
8563-3704	0.0192	8.63	3.79	1.52	+0.047 ± 0.007	+0.095 ± 0.007	ISOLATED
8987-6101	0.0219	8.63	5.10	2.04	−0.069 ± 0.008	−0.048 ± 0.006	ISOLATED
8241-6101	0.0209	8.63	5.82	2.33	+0.104 ± 0.038	+0.162 ± 0.040	DISTURBED
8566-6103	0.0103	8.64	4.69	1.88	−0.018 ± 0.005	+0.020 ± 0.009	ISOLATED
8564-1901	0.0196	8.64	3.35	1.34	+0.044 ± 0.008	+0.079 ± 0.011	DISTURBED
8439-1901	0.0164	8.65	3.21	1.28	+0.097 ± 0.007	+0.143 ± 0.006	ISOLATED
8135-6101	0.0109	8.65	6.84	2.74	+0.077 ± 0.016	+0.112 ± 0.014	DISTURBED
8936-6104	0.0142	8.65	6.16	2.46	+0.094 ± 0.017	+0.158 ± 0.020	DISTURBED
10517-12704	0.0132	8.66	9.39	3.76	−0.289 ± 0.132	−0.128 ± 0.107	DISTURBED
8991-3703	0.0191	8.66	4.41	1.77	−0.006 ± 0.004	+0.041 ± 0.004	ISOLATED
10496-12703	0.0189	8.66	12.05	4.82	−0.068 ± 0.009	−0.045 ± 0.008	DISTURBED
11977-12704	0.0211	8.66	10.06	4.02	−0.033 ± 0.015	+0.025 ± 0.022	DISTURBED
9001-9102	0.0214	8.66	2.64	1.05	+0.073 ± 0.003	+0.106 ± 0.005	ISOLATED
8567-6102	0.0227	8.66	3.81	1.52	+0.013 ± 0.008	+0.041 ± 0.011	DISTURBED
8552-6101	0.0180	8.66	6.54	2.62	−0.050 ± 0.010	−0.042 ± 0.005	DISTURBED
9485-9102	0.0188	8.67	7.91	3.16	−0.002 ± 0.011	−0.011 ± 0.007	DISTURBED
8716-12701	0.0190	8.67	7.45	2.98	−0.009 ± 0.001	−0.015 ± 0.002	DISTURBED
8987-6103	0.0217	8.67	7.52	3.01	−0.063 ± 0.007	−0.025 ± 0.011	ISOLATED
9500-3702	0.0216	8.68	4.60	1.84	+0.069 ± 0.010	+0.121 ± 0.015	DISTURBED
8323-12702	0.0230	8.68	8.99	3.60	+0.207 ± 0.052	+0.250 ± 0.054	ISOLATED
8551-6101	0.0188	8.68	7.30	2.92	−0.052 ± 0.008	−0.035 ± 0.005	DISTURBED

Notes. Sorted by stellar mass. Only the first 50 entries are shown here; the full table is available at the CDS. Columns give the MaNGA plate-IFU identifier, spectroscopic redshift, log stellar mass, effective radius, spatial resolution ratio R_e/θ_{PSF}, metallicity gradient slope with 1σ uncertainty, corrected residual metallicity gradient slope with 1σ uncertainty, and visual classification. Three galaxies (11020-12701, 8554-12704, 8150-3701) have catalogue redshifts below the nominal selection range $0.01 \leq z \leq 0.05$; see Sect. 3.2.